

# Mechanism of microtubule lumen entry for the $\alpha$ -tubulin acetyltransferase enzyme $\alpha$ TAT1

Courtney Coombes<sup>a</sup>, Ami Yamamoto<sup>a</sup>, Mark McClellan<sup>a</sup>, Taylor A. Reid<sup>a</sup>, Melissa Plooster<sup>a</sup>, G. W. Gant Luxton<sup>a</sup>, Joshua Alper<sup>b</sup>, Jonathon Howard<sup>c</sup>, and Melissa K. Gardner<sup>a,1</sup>

<sup>a</sup>Department of Genetics, Cell Biology, and Development, University of Minnesota, Minneapolis, MN 55455; <sup>b</sup>Department of Physics and Astronomy, Clemson University, Clemson, SC 29634; and <sup>c</sup>Department of Molecular Biophysics and Biochemistry, Yale University, New Haven, CT 06520

Edited by Eva Nogales, University of California, Berkeley, CA, and approved October 5, 2016 (received for review April 3, 2016)

**M**icrotubules are structural polymers inside of cells that are subject to posttranslational modifications. These posttranslational modifications create functionally distinct subsets of microtubule networks in the cell, and acetylation is the only modification that takes place in the hollow lumen of the microtubule. Although it is known that the  $\alpha$ -tubulin acetyltransferase ( $\alpha$ TAT1) is the primary enzyme responsible for microtubule acetylation, the mechanism for how  $\alpha$ TAT1 enters the microtubule lumen to access its acetylation sites is not well understood. By performing biochemical assays, fluorescence and electron microscopy experiments, and computational simulations, we found that  $\alpha$ TAT1 enters the microtubule lumen through the microtubule ends, and through bends or breaks in the lattice. Thus, microtubule structure is an important determinant in the acetylation process. In addition, once  $\alpha$ TAT1 enters the microtubule lumen, the mobility of  $\alpha$ TAT1 within the lumen is controlled by the affinity of  $\alpha$ TAT1 for its acetylation sites, due to the rapid rebinding of  $\alpha$ TAT1 onto highly concentrated  $\alpha$ -tubulin acetylation sites. These results have important implications for how acetylation could gradually accumulate on stable subsets of microtubules inside of the cell.

microtubule | acetylation | biophysics | microscopy | modeling

**M**icrotubules are dynamic structural polymers that participate in cell and organelle morphology and motility, intracellular transport, signaling, and chromosome movement during mitosis. Despite these various roles, microtubule structure is highly conserved: microtubules across a wide range of organisms are hollow tube structures that are made up of  $\alpha$ - and  $\beta$ -tubulin heterodimers stacked end-to-end into protofilaments. For microtubules to perform such a wide range of tasks, the cell uses a variety of posttranslational modifications to fine-tune their function (1, 2). Unlike the other known microtubule posttranslational modifications, the enzyme responsible for microtubule acetylation must access the  $\alpha$ -tubulin Lysine 40 (Lys40) site inside the hollow portion of the microtubule, known as the lumen, to acetylate microtubules (3, 4). Because of this unique localization to the lumen, the functional consequences of microtubule acetylation were initially puzzling to the field. However, recent functional studies have revealed effects of microtubule acetylation on cell signaling (5), cell cycle progression (6), and breast cancer cell migration (7). In humans, microtubule acetylation may be important for intracellular cargo transport in neurons and neuronal maintenance in neurodegenerative disease contexts, including Alzheimer's (8), Parkinson's (9, 10), and Huntington's (11) diseases.

The primary enzyme that is responsible for  $\alpha$ -tubulin Lys40 acetylation in mammals, nematodes, and protozoa has been identified as  $\alpha$ -tubulin acetyltransferase 1 ( $\alpha$ TAT1), which was first found in *Tetrahymena* and *Caenorhabditis elegans* (12–14). However, despite identification of the enzyme and its substrate, the mechanism for how  $\alpha$ TAT1 enters the microtubule lumen to access its acetylation sites is yet to be fully understood. There are several potential mechanisms for how  $\alpha$ TAT1 may access the acetylation site on the inside of the microtubule lumen: by copolymerization with tubulin at growing microtubule plus-ends (15), by transient openings in the lattice during microtubule breathing

(13, 16, 17), or by microtubule end-entry (12, 18). Copolymerization is not likely to be the primary mechanism for  $\alpha$ TAT1 access, because stable microtubules are acetylated, and because  $\alpha$ TAT1 is more active on polymerized microtubules than on free tubulin dimers (12, 13, 19–25). Conversely, the other modes of access are possible (12, 13, 18). Distinguishing among these possibilities is important for developing a mechanistic understanding to explain how  $\alpha$ TAT1 could access its acetylation sites to facilitate microtubule acetylation.

In this work, we found that  $\alpha$ TAT1 enters the microtubule lumen from the microtubule ends, and through breaks and bends in the lattice. Further, recent work suggested that  $\alpha$ TAT1 was able to diffuse efficiently within the microtubule lumen, and thus acetylate microtubules without a preference for microtubule ends (18). However, our results support a model in which the mobility of  $\alpha$ TAT1 within the lumen is controlled by the affinity of  $\alpha$ TAT1 for its acetylation sites, which are highly concentrated inside of the microtubule lumen, and in which the acetylation efficiency of  $\alpha$ TAT1 is regulated, in part, by the accessibility of acetylation sites through alterations in microtubule structure.

## Results

**$\alpha$ TAT1 Is Concentrated Near to Microtubule Ends.** To investigate the localization of  $\alpha$ TAT1 binding to the microtubule, we used total internal reflection fluorescence (TIRF) microscopy to visualize the interactions of purified  $\alpha$ TAT1-GFP protein (*SI Appendix*, Fig. S1A) with guanosine-5'-[ $(\alpha,\beta)$ -methylene]triphosphate (GMPCPP)-stabilized (nondynamic), rhodamine-labeled microtubules (13). Here, purified tubulin was combined with the slowly hydrolyzable GTP analog, GMPCPP, and incubated for 2 h. The resulting

## Significance

**$\alpha$ TAT1 is an enzyme that acetylates microtubules inside of cells, and acetylation is an important posttranslational microtubule modification. However, microtubules are long tubes, and the acetylation site for  $\alpha$ TAT1 is on the inside of this tube. We investigated how  $\alpha$ TAT1 enters the microtubule and moves around to access its acetylation sites once inside. We found that  $\alpha$ TAT1 enters microtubules through its ends but does not move efficiently inside of the microtubule. However, a lowered affinity allows the enzyme to move more efficiently and leads to longer stretches of acetylation. Therefore, acetylation of microtubules could be controlled in the cell by modulating the affinity of  $\alpha$ TAT1 for its acetylation site or increasing the number of microtubule ends.**

Author contributions: C.C., M.M., G.W.G.L., J.A., J.H., and M.K.G. designed research; C.C., A.Y., M.M., and M.P. performed research; M.M., T.A.R., and M.K.G. contributed new reagents/analytic tools; C.C., A.Y., M.M., and M.K.G. analyzed data; and C.C. and M.K.G. wrote the paper. The authors declare no conflict of interest.

This article is a PNAS Direct Submission.

<sup>1</sup>To whom correspondence should be addressed. Email: klei0091@umn.edu.

This article contains supporting information online at [www.pnas.org/lookup/suppl/doi:10.1073/pnas.1605397113/-DCSupplemental](http://www.pnas.org/lookup/suppl/doi:10.1073/pnas.1605397113/-DCSupplemental).

microtubules were then attached to a coverslip in an imaging chamber using antirhodamine antibody, and 30 nM  $\alpha$ TAT1-GFP (*SI Appendix*, Fig. S1A and C) in imaging buffer was then introduced to the imaging chamber (*SI Appendix*). After steady-state binding was achieved (~20 min; *SI Appendix*, Fig. S1B), single-time-point images were collected using TIRF microscopy (Fig. 1A). Qualitatively, we observed that  $\alpha$ TAT1-GFP was concentrated near to the microtubule ends (Fig. 1B, Top; typical images). We then quantified the microtubule images, and the corresponding green  $\alpha$ TAT1-GFP fluorescence, by plotting the average red tubulin and green  $\alpha$ TAT1-GFP fluorescence intensity as a function of the distance from the highest red fluorescence intensity (bright) microtubule end to the lowest red fluorescence intensity (dim) microtubule end [Fig. 1B, Bottom (red, microtubule; gray,  $\alpha$ TAT1-GFP) and *SI Appendix*, Fig. S2A]. Here, the “dim” end of the microtubule is likely composed of variable protofilament lengths (26–28), and thus may expose the internal microtubule luminal surface (Fig. 1B, cartoon), an effect that may be enhanced by the microtubule depolymerizing properties of  $\alpha$ TAT1 (29) (*SI Appendix*, Fig. S2C). We then normalized the green  $\alpha$ TAT1-GFP fluorescence intensity to its

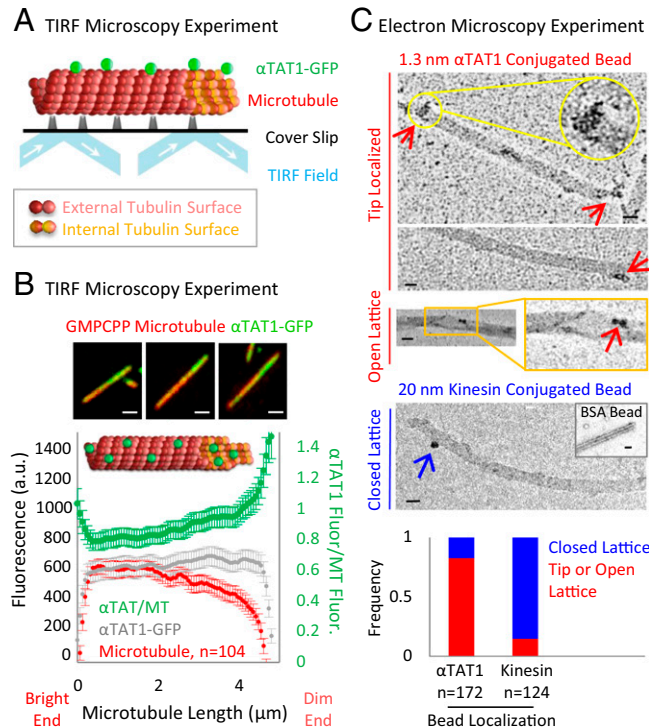


**Fig. 1.**  $\alpha$ TAT1 preferentially targets the dim microtubule ends of GMPCPP-stabilized microtubules. (A) TIRF microscopy experiments to characterize  $\alpha$ TAT1-GFP localization (green) on microtubules (red). (B, Top) Typical images of  $\alpha$ TAT1-GFP binding (green) to rhodamine-labeled GMPCPP microtubules (red). (Scale bars: 1  $\mu$ m.) (B, Bottom) Quantitative average fluorescence line scans indicating the localization of  $\alpha$ TAT1-GFP on microtubules [ $n = 104$  microtubules, error bars illustrate 95% confidence intervals, and green markers are  $\alpha$ TAT-GFP intensity (gray) normalized to microtubule intensity (red) at each position]. Data from other microtubule lengths are shown in *SI Appendix*, Fig. S1C. (Inset) Cartoon demonstrates the preferential localization of  $\alpha$ TAT1-GFP to the dim microtubule end. (C, Top) TEM images of  $\alpha$ TAT1 conjugated to a 1.3-nm gold bead (red arrows point to  $\alpha$ TAT bead clusters at tips and open microtubule lattice). (C, Middle) TEM images of monomeric kinesin-1 conjugated to a 20-nm gold bead (blue arrow points to a kinesin bead on the microtubule lattice). (Inset) BSA conjugated to 1.3-nm gold beads with stabilized GMPCPP microtubules. (Scale bars: 25 nm.) (C, Bottom) Quantification for localization of  $\alpha$ TAT1 beads compared with kinesin beads. au, arbitrary units; Fluor, fluorescence, MT, microtubule.

corresponding red microtubule fluorescence intensity at each microtubule position (Fig. 1B, Bottom; green markers) to account for reduced total tubulin polymer at the dim microtubule end. We found that the normalized  $\alpha$ TAT1-GFP concentration was higher at microtubule ends, and especially on the dim end of the microtubule, which suggests that  $\alpha$ TAT1 is concentrated on exposed luminal sites at open, tapered microtubule ends (Fig. 1B and *SI Appendix*, Fig. S2). To test whether less tapered, “blunt” microtubule tips had reduced targeting of  $\alpha$ TAT1-GFP to their ends, we generated a new population of microtubules that were grown for a shorter amount of time (~10 min), which allowed us to analyze microtubules with reduced taper at the microtubule end (*SI Appendix*, Fig. S2B). Consistent with the idea that open, tapered microtubule ends with exposed acetylation sites more readily bind  $\alpha$ TAT1 as compared to closed, blunt ends, we observed reduced targeting of  $\alpha$ TAT1-GFP on the blunt microtubule tips (*SI Appendix*, Fig. S2B).

To confirm that  $\alpha$ TAT1 binding was concentrated in areas of the microtubule with exposed luminal sites, we conjugated purified, unlabeled  $\alpha$ TAT1 (*SI Appendix*, Fig. S1A) to 1.3-nm-diameter gold beads, incubated the  $\alpha$ TAT1-conjugated beads with GMPCPP-stabilized microtubules for 20 min, and then imaged the microtubules using transmission electron microscopy (TEM) (*SI Appendix*). The 1.3-nm-diameter beads act as reporters for  $\alpha$ TAT1 localization, but they should not limit access to the lumen because they are smaller than the inner diameter of the microtubule (~15 nm). Consistent with the  $\alpha$ TAT1-GFP fluorescence data, 86% of the observed  $\alpha$ TAT1-conjugated bead clusters were located either at open microtubule ends or at breaks or openings in the lattice (Fig. 1C, Top; red arrows and bars). This result is in contrast to BSA-conjugated control beads, in which 83% of BSA beads did not bind microtubules at all (Fig. 1C, Middle; black Inset), and of the remainder of the BSA beads, 13% were bound to the lattice and 4% to microtubule ends. For a positive control, we then conjugated monomeric (truncated) kinesin-1 to beads, mixed the kinesin beads with microtubules in the presence of adenylyl-imidodiphosphate (AMPPNP) to allow for rigor binding, and then imaged the kinesin beads and microtubules using TEM (30) (Fig. 1C, Middle; blue arrow and bar). We then directly compared the localization of the  $\alpha$ TAT1-conjugated beads with the stationary kinesin-conjugated beads (Fig. 1C, Bottom), and found that although 86% of the bound  $\alpha$ TAT1 beads were at microtubule tips or defects, only 15% of the kinesin beads were at tips or defects, with the remainder of the kinesin beads (85%) bound to the closed lattice (Fig. 1C). This finding suggests that  $\alpha$ TAT1 specifically targeted the beads to open microtubule ends and lattice openings.

**Simulations Suggest  $\alpha$ TAT1-GFP End-Entry into the Microtubule Lumen.** To investigate whether the experimentally observed  $\alpha$ TAT1-GFP localization on stabilized microtubules could correlate with a lumen entry mechanism, we performed computational simulations of the  $\alpha$ TAT1-microtubule interaction. Our simulations accounted for the (i) association and dissociation of  $\alpha$ TAT1 with tubulin subunits on the external surface of the lattice, and diffusion of  $\alpha$ TAT1 on this surface (Fig. 2A, Left; *SI Appendix*; and *SI Appendix*, Fig. S3), (ii) association and dissociation of  $\alpha$ TAT1 on the internal luminal surface of the microtubule and diffusion in solution within the lumen (Fig. 2A, Center), and (iii) adjusting of the simulated microtubule tip structures to match experimentally observed average microtubule-associated fluorescence line scans (Fig. 2A, Right). We constrained our model parameters either through experiments (*SI Appendix*, Fig. S3), or, alternatively, by testing them over a range of values to ensure that model conclusions did not depend on narrowly defined parameter values (*SI Appendix*, Fig. S3). We found that the modeling results for  $\alpha$ TAT1-GFP localization on microtubules were most sensitive to the parameter  $\gamma$ , which controls the  $\alpha$ TAT1 off-rate (affinity) on the luminal surface of the microtubule, as described below.

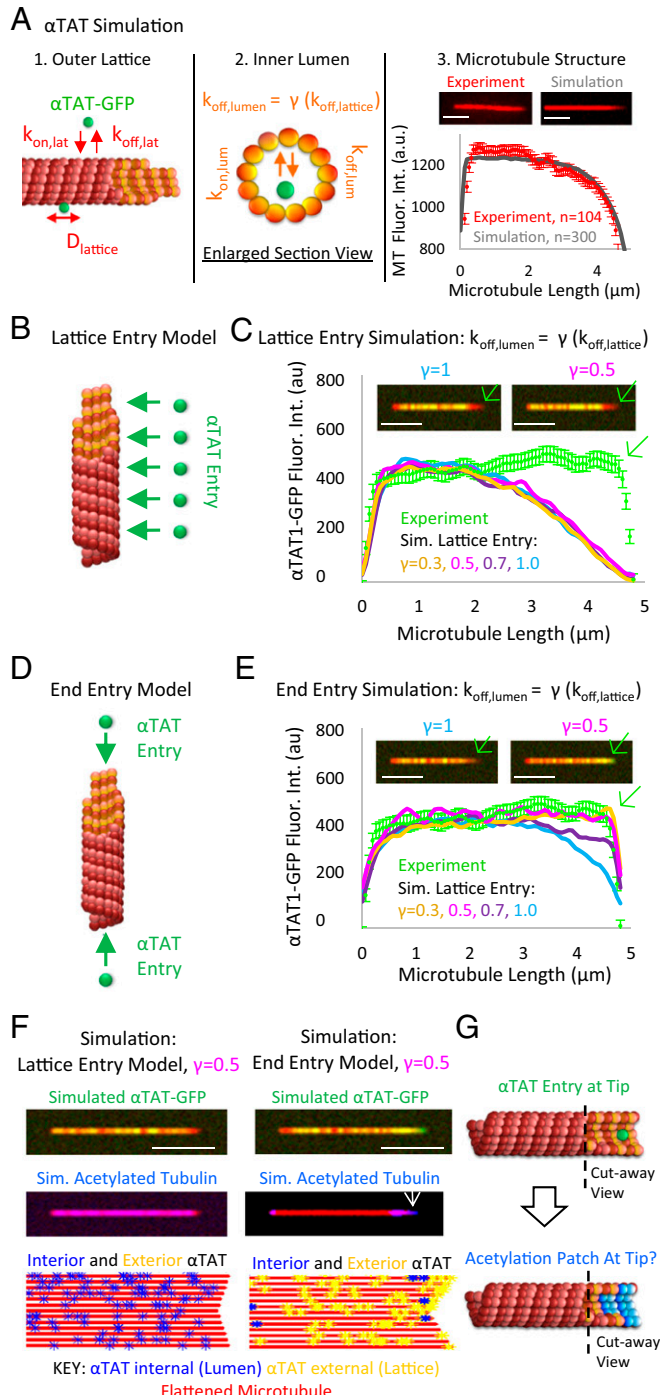


**Fig. 2.** Simulations predict differential acetylation patterns based on the  $\alpha$ TAT1 microtubule entry model. (A) Rules for  $\alpha$ TAT1 simulation, which include (i) movement and binding of  $\alpha$ TAT1 on the external surface of the microtubule (Left), (ii) binding and unbinding of  $\alpha$ TAT1 on the inside surface of the microtubule (Center), and (iii) adjusting of simulated microtubule (MT) tip structure to match experimental fluorescence line scale profiles (Right). (B) In the simulated  $\alpha$ TAT1 lattice entry model,  $\alpha$ TAT1 is able to enter the lumen randomly at any point along the microtubule. (C) Lattice-entry model does not reproduce experimental  $\alpha$ TAT1-GFP localization results, regardless of the value for  $\gamma$ . (D) In the simulated  $\alpha$ TAT1 end-entry model,  $\alpha$ TAT1 is only able to enter the microtubule lumen from its ends. (E) End-entry model reproduces experimental  $\alpha$ TAT1-GFP localization results if  $\gamma \leq 0.5$ . (F) Simulated  $\alpha$ TAT1-GFP localization (Top), the resulting distribution of acetylated tubulin (Middle), and a cartoon of resulting locations of simulated  $\alpha$ TAT1 molecules (Bottom), when using the lattice entry model (Left) and end entry model (Right) (also **Movies S1** and **S2**). (G) Luminal  $\alpha$ TAT1 (green) diffuses in solution

We then used the simulation to predict  $\alpha$ TAT1-GFP localization for two potential models that explain how  $\alpha$ TAT1 could enter into the microtubule lumen (end vs. lattice entry). We first tested a microtubule “lattice entry” model in which simulated  $\alpha$ TAT1 could bind the microtubule lattice, and then subsequently enter into the lumen regardless of its position along the microtubule (Fig. 2B), similar to a “breathing” model in which transient lattice openings could routinely provide access for  $\alpha$ TAT1 to enter the lumen along the length of the lattice. Using the lattice entry model, the simulated  $\alpha$ TAT1-GFP localization data were not consistent with the experimentally observed localization of  $\alpha$ TAT1-GFP at the microtubule tip (Fig. 2C). We ran this simulation for multiple values of  $\gamma$ , which is the relative affinity of  $\alpha$ TAT1 for  $\alpha$ -tubulin Lys40 acetylation sites on the inside surface versus the outside of the microtubule [ $k_{off,lumen} = \gamma(k_{off,lattice})$ ]. We found that the lattice entry model failed to explain the experimental data, regardless of the value for  $\gamma$  (Fig. 2C).

Next, we used our simulations to test a microtubule “end-entry” model, in which simulated  $\alpha$ TAT1 could only enter the lumen through the microtubule ends (Fig. 2D). The simulated  $\alpha$ TAT1-GFP localization data were consistent with the experimentally observed localization of  $\alpha$ TAT1-GFP at the microtubule tip for  $\gamma \leq 0.5$  ( $k_{off,lumen} = 0.5$  per second; Fig. 2E), meaning that the simulated localization of  $\alpha$ TAT1-GFP on stabilized microtubules was consistent with the experiment if (i)  $\alpha$ TAT1 entered the lumen at microtubule ends and (ii) the simulated off-rate of  $\alpha$ TAT1 was twofold higher on the outside of the lattice relative to its acetylation site on the luminal surface of the microtubule (i.e.,  $k_{off,lumen} = 0.5$  per second).

Thus, the results from these simulations suggest that the primary mode of  $\alpha$ TAT1 entry into the lumen is through the microtubule ends, and that the affinity of  $\alpha$ TAT1 for the  $\alpha$ -tubulin Lys40 acetylation sites within the lumen is higher than its affinity for the outside of the microtubule. However, our  $\alpha$ TAT1-GFP localization studies could not differentiate whether the experimentally observed  $\alpha$ TAT1-GFP molecules were on the inside or the outside of the microtubule (Fig. 1B). Therefore, we used the simulation to predict the pattern of acetylation on the inside of a stabilized microtubule, as would be visualized using a fluorescent antiacetylated tubulin antibody. We found that the lattice-entry model predicted uniformly distributed acetylated tubulin subunits along the length of the microtubule (Fig. 2F, *Left Middle* and **Movie S1**) because the  $\alpha$ TAT1 molecules that entered the lumen along the length of the microtubule lattice were randomly localized along the inside of the microtubule (Fig. 2F, *Left Bottom*; cartoon). Conversely, we found that the end-entry simulation predicted concentrated, short “patches” of acetylation at microtubule ends (Fig. 2F, *Right Middle* and **Movie S2**). These patches were predicted because the  $\alpha$ TAT1 molecules that entered the lumen through the microtubule ends tended to remain near to the microtubule ends (Fig. 2F, *Right Bottom*; cartoon).

In the end-entry  $\alpha$ TAT1 simulation, the luminal  $\alpha$ TAT1 molecules remained near to the microtubule ends because the simulated  $\alpha$ TAT1 molecules exhibited very slow mobility inside of the microtubule lumen. Although it is expected that  $\alpha$ TAT1 should diffuse rapidly in solution within the lumen, the concentration of  $\alpha$ -tubulin Lys40 binding sites inside of the lumen is very high due to the small volume and dense packing of tubulin subunits inside the lumen (~17 mM; calculated in **SI Appendix**). This high concentration of  $\alpha$ -tubulin Lys40 binding sites within the lumen makes the effective on-rate for an individual  $\alpha$ TAT1 molecule inside of a microtubule also very high. For example, we predict that the typical rebinding time for a free  $\alpha$ TAT1 molecule inside the lumen will be

but rapidly rebinds to nearby tubulin subunits. (Top) Thus,  $\alpha$ TAT1 moves slowly down the lumen. (Bottom) As a result, the simulation predicts patches of acetylated tubulin near to the microtubule end (blue, acetylated subunits) (Scale bars: 3  $\mu$ m.) Int., intensity; Sim., simulated.

$(1/(k_{on}[\text{binding sites}])) = 6 \times 10^{-5}$  per second (using a diffusion-limited biomolecular on-rate constant of  $k_{on} = 1 \mu\text{M}^{-1}\cdot\text{s}^{-1}$ ) (31). As a result, we further predict that the root mean squared travel distance for a free  $\alpha$ TAT1 molecule before rebinding to an  $\alpha$ -tubulin Lys40 acetylation site ( $\Delta x_{lumen}$ ) would be  $\sim 50$  nm, where

$$\langle \Delta x_{lumen}^2 \rangle^{1/2} = \sqrt{2D_{lumen} \Delta t_{rebind}}, \quad [1]$$

in which  $D_{lumen}$  is the  $\alpha$ TAT1 diffusion coefficient in solution ( $\sim 2.6 \times 10^{-7} \text{ nm}^2\cdot\text{s}^{-1}$ ) (18) and  $\Delta t_{rebind}$  is the typical rebinding time, as calculated above ( $\sim 6 \times 10^{-5} \text{ s}^{-1}$ ). This predicted mean travel distance is similar to previous computational predictions (32).

Thus, the end-entry model for  $\alpha$ TAT1 predicts that there will be patches of acetylated tubulin near to the  $\alpha$ TAT1 entry point at microtubule ends because the mobility of  $\alpha$ TAT1 within the lumen may be limited by rapid rebinding of luminal  $\alpha$ TAT1 to nearby tubulin subunits (Fig. 2G), with patch length further limited by a slow luminal off-rate (SI Appendix, Fig. S3C; simulated  $k_{off,lumen} = 0.5$  per second). This behavior led to two key predictions from the simulation that could be tested experimentally. First, if the end-entry model is correct, then acetylation should be most commonly observed near to the ends of the microtubules, where  $\alpha$ TAT1 routinely enters the lumen. Second, if there is slow mobility of  $\alpha$ TAT1 inside of the microtubule lumen due to rapid rebinding, then concentrated patches of microtubule acetylation should be observed, rather than a uniform dispersion of acetylation along the length of the microtubule (Fig. 2G).

**Microtubule Acetylation Occurs in Patches at Microtubule Ends.** We experimentally tested these simulation predictions by visualizing fluorescently labeled antiacetylated tubulin antibodies on rhodamine-labeled, GMPCPP-stabilized microtubules. Here, GMPCPP-stabilized microtubules were adhered to flow chamber coverslips as described above. A mixture of  $2.5 \mu\text{M}$  unlabeled  $\alpha$ TAT1,  $2 \text{ mM}$  acetyl CoA (AcCoA), and Brb80 was then introduced into the imaging chamber and incubated with the coverslip-adhered microtubules for 30 min (Fig. 3A, Left). Then, the  $\alpha$ TAT1 mixture was gently flushed from the chamber, and imaging buffer with CF488-labeled antiacetylated tubulin antibody was introduced to the chamber. The fluorescent antiacetylated tubulin antibody and microtubules were then imaged using TIRF microscopy (Fig. 3A, Left and Materials and Methods). We observed acetylation patches at the ends of microtubules (Fig. 3A, Right Top), similar to the simulation predictions for the end-entry model (Fig. 2F, Right; white arrow). The patches, which were defined as an area of fluorescent antibody localization along the length of the microtubule lattice, averaged  $\sim 300$  nm in length. This length represents up to  $\sim 200$  acetylated tubulin subunits [ $= ((300 \text{ nm} - 170 \text{ nm point spread function})/(8 \text{ nm}/\text{layer})) * (13 subunits}/\text{layer}$ ]. Less frequently, we also observed patches within the microtubule lattice (Fig. 3A, Right Bottom). To quantify this observation, we calculated the patch frequency per site by normalizing the patch frequency to the number of available sites in each case, where end sites represented the last 128 nm (two pixels) of a microtubule at each end and lattice sites represented the remainder of the microtubule. Similar to the predictions from our simulation, we found that patches were 15-fold more likely to occupy microtubule end sites than microtubule lattice sites (Fig. 3B; binomial test,  $P < 2 \times 10^{-6}$ ). Further, we measured the fluorescence intensity of the microtubule lattice at internal acetylation spots, and, consistent with the idea that internal acetylation may be correlated with broken microtubules, defects, or distinct microtubule ends, internal patches of acetylation were more frequently localized to dim areas on the microtubule compared with the mean microtubule brightness (Fig. 3B, Inset; binomial test,  $P = 3.4 \times 10^{-5}$ ).

To ensure that the antibody itself was not limited in its mobility to travel within the lumen, leading to an inability to detect

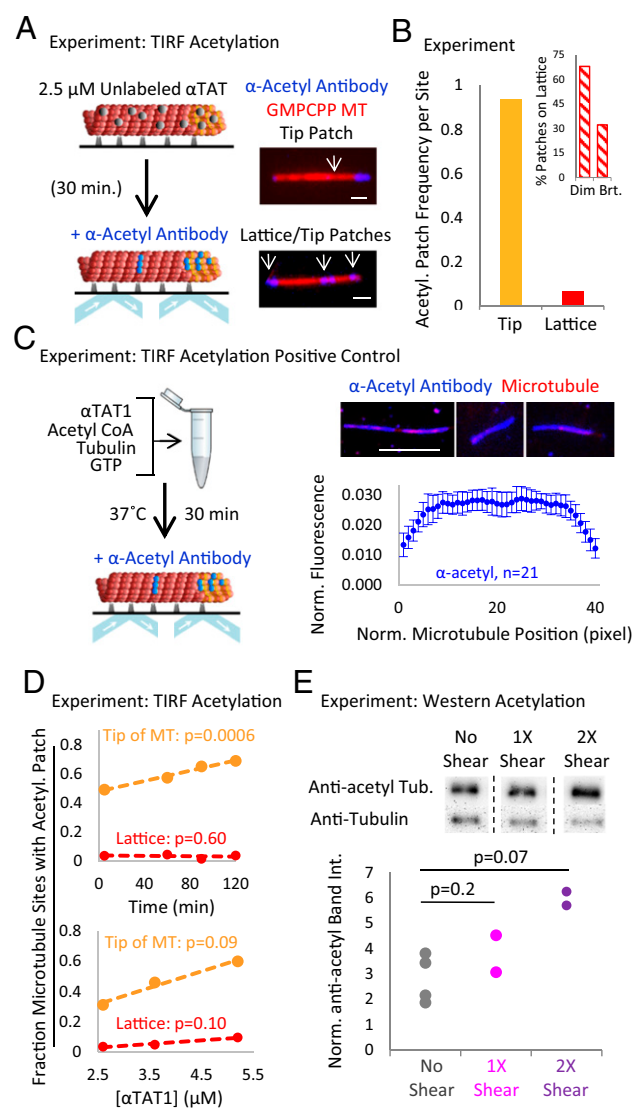


**Fig. 3.** Acetylation occurs in patches, which are preferentially localized at microtubule ends. (A, Left) Schematic of acetylation TIRF experiment. (A, Right) Typical images of acetylated microtubules. (Scale bars:  $1 \mu\text{m}$ .) (B) Patch frequency per site ( $n = 426$  microtubules). (Inset) Acetylation patches within the lattice were more likely to occur on dim areas of the microtubule. (C, Left) Schematic of positive control assay. (C, Right Top) Typical images of fully acetylated microtubules. (Scale bar:  $3 \mu\text{m}$ .) (C, Right Bottom) Quantification of average  $\alpha$ -acetyl antibody fluorescence along the length of fully acetylated microtubules of similar length. (D) Acetylation patch frequency by location on preformed, stabilized microtubules with increasing amounts of  $\alpha$ TAT1 incubation time ( $2.5 \mu\text{M}$   $\alpha$ TAT1, Top) or increasing concentrations of  $\alpha$ TAT1 (30 min of  $\alpha$ TAT1 incubation time, Bottom). To maintain consistency, the preparation of microtubules was held common within each of the experiments that measured acetylation with increasing time or concentration. (E) Results for microtubule shearing experiment as measured with Western blots. (Error bars in all panels are 95% confidence intervals, and  $P$  values are shown for comparison with same time point unsheared controls in each case). Acetyl., acetylated; Brt, bright; Norm., normalized; Tub, tubulin.

acetylation along the length of the microtubules, we performed a positive control experiment. Here, dynamic microtubules were grown in the presence of  $\alpha$ TAT1 and AcCoA, in contrast to the stabilized microtubule experiments above, in which  $\alpha$ TAT1 and AcCoA were added to preformed microtubules (Fig. 3C, Left vs. Fig. 3A). After 30 min of growth and acetylation, the dynamic microtubules were then stabilized with Taxol, introduced to an

imaging chamber, and imaged with the fluorescent antiacetylated tubulin antibody (Fig. 3C, *Left*). We observed a population of microtubules that were uniformly labeled with antibody over their entire lengths (Fig. 3C, *Right Top*), indicating that the antibody was indeed able to access a uniform proportion of the acetylated sites in the microtubules. To quantify this observation, average line scans for similar length, fully acetylated microtubules in the positive controls were collected. We found that the antibody brightness was uniform along the length of the microtubule for the fully acetylated controls (Fig. 3C, *Right Bottom*), indicating that the fluorescent antibody brightness as visualized by TIRF microscopy was similar whether the antibody reported acetylated tubulin subunits near to the ends of the microtubules or inside of the lumen along the length of the microtubule.

**Acetylation at Microtubule Ends Increases over Time.** To test whether increased  $\alpha$ TAT1 incubation time would increase the frequency of the acetylation patches, we incubated stable, preformed microtubules with 2.5  $\mu$ M  $\alpha$ TAT1 for times ranging from 5 to 120 min and then visualized microtubule acetylation with fluorescent antiacetylation antibody. We found that the fraction of microtubules with acetylation patches at their ends increased over time (Fig. 3D, *Top* and *SI Appendix, Fig. S4B*), and we note that a similar trend was observed with increasing  $\alpha$ TAT1 concentrations in which incubation time was held constant at 30 min (Fig. 3D, *Bottom* and *SI Appendix, Fig. S4A*). Thus, increasing the  $\alpha$ TAT1 incubation time (Fig. 3D, *Top*) or concentration (Fig. 3D, *Bottom*) led to a higher overall acetylation level due, in part, to an increased fraction of acetylated microtubule ends, consistent with an end-entry model. As indicated by the nonzero intercept in the frequency graphs in Fig. 3D (*Top*), we noted that a fraction of the microtubules displayed acetylation patches at their ends very quickly, followed by a slower increase over time for the remainder of the microtubules ( $P = 0.0006$ , linear regression). We hypothesize that the fraction of microtubule ends that were very quickly acetylated had readily accessible acetylation sites (e.g., via open, tapered ends), whereas the more slowly acetylated ends required rate-limiting entry of  $\alpha$ TAT1 into the microtubule through blunt ends, consistent with our observation that tapered microtubule ends have increased targeting of  $\alpha$ TAT1-GFP relative to blunt ends (Fig. 1B vs. *SI Appendix, Fig. S2B*).

If higher acetylation levels over time were due, in part, to an increased number of acetylated microtubule ends, and particularly to an increased number of tapered or opened microtubule ends, we reasoned that bulk acetylation levels would increase if the number of microtubule ends and/or lattice openings were increased by mechanical shearing and breaking of the microtubules. To test this prediction, we mixed rhodamine-labeled, GMPCPP-stabilized microtubules with unlabeled  $\alpha$ TAT1, separated half of the mixture, and sheared it using a small-diameter needle (1 $\times$  shear). After a 120-min incubation time, we sheared a portion of the 1 $\times$  mixture a second time (2 $\times$  shear), and then allowed the 2 $\times$  shear mixture to incubate for an additional 60 min. We quantified the acetylation levels for both mixtures using western blots, and then normalized each antiacetylation band intensity to its tubulin loading control to account for loss of microtubules inside of the syringe during the shearing process (Fig. 3E, *Top*). We found that the microtubule acetylation levels were slightly higher for the 1 $\times$  sheared mixture relative to its nonsheared control ( $P = 0.2$ ) and that the 2 $\times$  sheared mixture was substantially more acetylated than its unsheared control ( $P = 0.07$ ; Fig. 3E, *Bottom*). This finding suggests that the microtubules were broken into smaller fragments and/or damaged by successive cycles of shearing, which generated new microtubule ends and/or openings in the lattice during each cycle, and thus allowed for more acetylated microtubule ends and/or lattice openings. The increase in acetylated microtubule ends then led to a higher bulk acetylation level (16). Thus, microtubule acetylation may be facilitated by increased numbers of microtubule ends or new lattice openings.

**Microtubule Acetylation Is Facilitated by New Lattice Openings.** In addition to mechanical shearing, another method for allowing access of  $\alpha$ TAT1 to the microtubule lumen may be by introducing large breaks or openings within the microtubule wall (Fig. 4A). Thus, we predicted that by opening up the closed tube, or by introducing breaks into the tube, increased numbers of acetylation patches would be observed along the length of the microtubule lattice, and there would be an increase in the bulk acetylation level of a microtubule population (Fig. 4B).

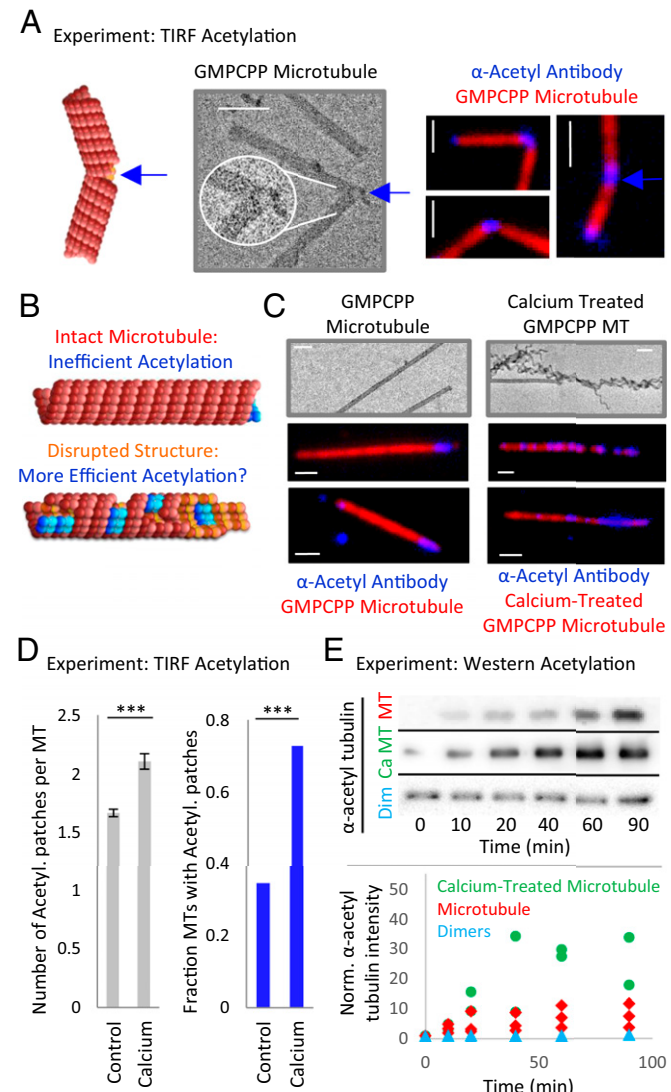


**Fig. 4.** Disruption of microtubule structure is correlated with higher acetylation rates. (A, *Left*) Schematic and TEM image of microtubule break at a bend. (Scale bar: 100 nm.) (A, *Right*) Acetylation-TIRF microscopy images of bent microtubules. (Scale bars: 1  $\mu$ m.) (B) If  $\alpha$ TAT1 typically enters the microtubule through its ends (*Top*), then the presence of new openings in the lattice may increase the acetylation rate (*Bottom*). (C, *Top*) TEM images of GMPCPP microtubules (*Left*), and  $\text{CaCl}_2$ -treated GMPCPP microtubules (*Right*). (Scale bars: 100 nm.) (C, *Middle* and *Bottom*) TIRF microscopy images of acetylated GMPCPP and  $\text{CaCl}_2$ -treated GMPCPP microtubules. (Scale bars: 1  $\mu$ m.) (D, *Left*) Mean number of patches per microtubule in control vs.  $\text{CaCl}_2$ -treated microtubules (control:  $n = 3,533$ , SD = 0.98;  $\text{CaCl}_2$ :  $n = 2,540$ , SD = 1.46). \*\*\* $P < 2 \times 10^{-6}$ . (D, *Right*) Fraction of microtubules that had at least one patch (control:  $n = 3,533$ ,  $\text{CaCl}_2$ :  $n = 2,540$ ). (E, *Top*) Representative western blots of acetylated dimers, GMPCPP microtubules, and  $\text{CaCl}_2$ -treated GMPCPP microtubules taken after 0–90 min of  $\alpha$ TAT1 incubation (also *SI Appendix, Fig. S4E*). (E, *Bottom*) Normalized western band intensities.

It has been previously demonstrated that opened, damaged microtubules can be created by briefly exposing GMPCPP microtubules to calcium (33). Therefore, rhodamine-labeled GMPCPP microtubules were briefly incubated with 40 mM CaCl<sub>2</sub>, and the CaCl<sub>2</sub>-treated microtubules were imaged with TEM (Fig. 4C, Top and SI Appendix). From the TEM images, it was clear that portions of the GMPCPP microtubules were opened and/or damaged through the CaCl<sub>2</sub> treatment (Fig. 4C, Top), which should allow increased access of  $\alpha$ TAT1 to its acetylation site inside the microtubule lumen. Therefore, coverslip-adhered CaCl<sub>2</sub>-treated microtubules were incubated with unlabeled  $\alpha$ TAT1 in an imaging chamber for 30 min, and acetylation was then imaged with anti-acetylated tubulin antibody (Fig. 4C, Bottom). We found that CaCl<sub>2</sub> treatment substantially increased both the number of patches per microtubule (Poisson regression,  $P < 2.2 \times 10^{-16}$ ) and the fraction of microtubules with patches (two-sample test of proportions,  $P < 2.2 \times 10^{-16}$ ) (Fig. 4D and SI Appendix, Fig. S4F).

To confirm that the antiacetylated tubulin antibody was properly reporting the acetylation of CaCl<sub>2</sub>-treated microtubules, we performed a parallel experiment using western blots. Acetylated tubulin levels were measured over time for control and CaCl<sub>2</sub>-treated microtubules (Fig. 4E, Top and SI Appendix, Fig. S4E), and the normalized band intensities were plotted as a function of  $\alpha$ TAT1 incubation time (Fig. 4E, Bottom). We found that the  $\alpha$ TAT1 acetylation level after 60–90 min of  $\alpha$ TAT1 incubation time was 3.7-fold higher for CaCl<sub>2</sub>-treated microtubules compared with control microtubules [Fig. 4E; green, CaCl<sub>2</sub>; red, controls (also plotted alone in SI Appendix, Fig. S1C); log-transformed linear regression,  $P = 0.003$ ], consistent with our fluorescence studies (Fig. 4D). In addition, we found that  $\alpha$ TAT1 does not acetylate tubulin dimers as efficiently as it does intact microtubules, consistent with previous  $\alpha$ TAT1 studies (18, 19) (Fig. 4E, blue).

Together, these results are consistent with the prediction that  $\alpha$ TAT1 relies on microtubule ends and breaks or openings in the microtubule lattice to allow access to the lumen.

**$\alpha$ TAT1 Exhibits Impeded Mobility Inside of the Microtubule Lumen.** Acetylation of stable microtubules may be limited both by  $\alpha$ TAT1 entry into the lumen and by  $\alpha$ TAT1 mobility within the lumen. To test  $\alpha$ TAT1 mobility within the lumen, stabilized microtubules were incubated with  $\alpha$ TAT1 for 5 or 120 min, and acetylation was visualized with fluorescently labeled antibody using TIRF microscopy as described above (Fig. 5A, Left). The overall increase in the fraction of acetylated tubulin subunits per (acetylated) microtubule was then assessed by reporting the acetylation patch lengths on individual microtubules, normalized to microtubule length. We found that the fraction of acetylation per microtubule increased slightly but significantly when the  $\alpha$ TAT1 incubation time was increased from 5 to 120 min (Fig. 5A, Middle). We found a similar small increase when the  $\alpha$ TAT1 concentration was increased from 2.5 to 3.5  $\mu$ M (Fig. 5A, Right;  $\alpha$ TAT1 incubation time of 30 min). This finding suggests that  $\alpha$ TAT1 is able to acetylate new tubulin subunits continually within the lumen, but at a slow pace. The slow pace of acetylation may be due, in part, to slow diffusion of  $\alpha$ TAT1 within the lumen, although, as previously reported (29), the presence of  $\alpha$ TAT1 leads to slow microtubule depolymerization (SI Appendix, Figs. S2C and S4 C and D), which also likely causes preferential loss of acetylation patches at microtubule tips over time, leading to an underestimate of patch length growth over time.

Thus, to measure the mobility of  $\alpha$ TAT1 within the microtubule lumen more directly, 15 nM  $\alpha$ TAT1-GFP protein was added to an imaging chamber with stabilized microtubules, and single-molecule movies were then collected using fast time-lapse TIRF microscopy (20 frames per second). We observed both slow- and fast-moving  $\alpha$ TAT1-GFP molecules (Fig. 5B, Left), which led to a wide range of measured diffusion coefficients (Fig. 5C, pink circles). We predicted that there may be a wide range of diffusion coefficients because, although many of the  $\alpha$ TAT1-GFP

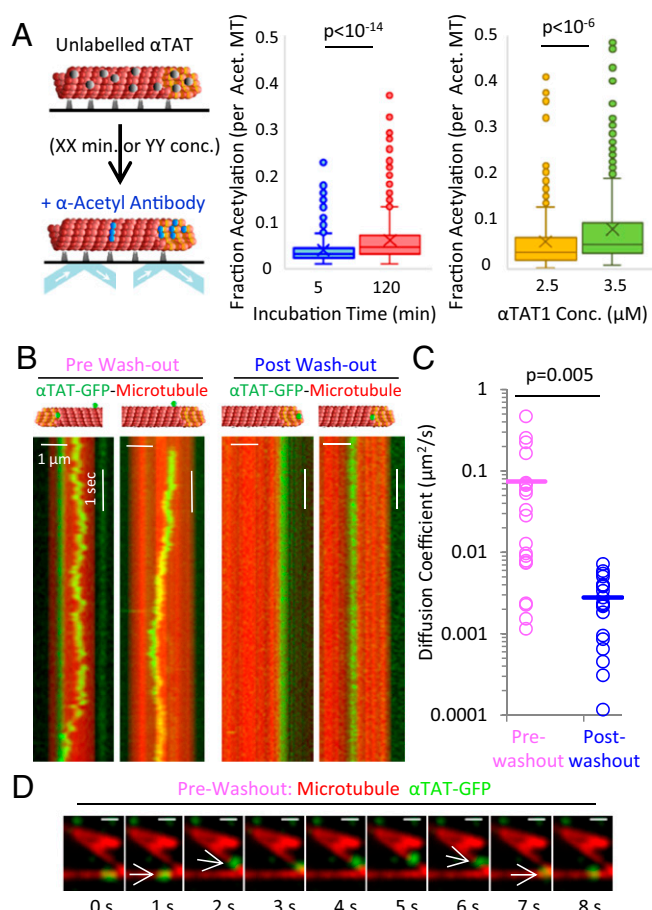


**Fig. 5.**  $\alpha$ TAT1 exhibits slow mobility within the lumen. (A, Left) Schematic of acetylation TIRF experiment. (A, Right) Fraction of acetylated tubulin on acetylated microtubules with short and long  $\alpha$ TAT1 incubation times (2.5  $\mu$ M  $\alpha$ TAT1) and low and high  $\alpha$ TAT1 concentrations (30-min incubation), all normalized to individual microtubule lengths. In the plot, the first and third quartiles are at the ends of the box, the line in the center of the box is the median, the marker inside the box is the mean, and the markers outside of the box represent outliers above the first and third quartiles. Conc., concentration. (B) Kymographs of  $\alpha$ TAT1 diffusion on GMPCPP microtubules before (Left) and after (Right) washout with buffer. (C) Diffusion coefficients for  $\alpha$ TAT1-GFP molecules imaged before (pink circles) or after (blue circles) washout. (D) Image panel from Movie S3 of  $\alpha$ TAT1-GFP diffusion on microtubule lattice before washout. The white arrows pointing to an  $\alpha$ TAT1-GFP molecule jumping from one microtubule to another suggest external lattice diffusion. (Scale bars: 500 nm.)

molecules were bound to and diffusing on the outer lattice (16), some of the  $\alpha$ TAT1-GFP molecules could have entered the microtubule lumen; thus, these molecules would reflect the mobility of  $\alpha$ TAT1-GFP within the lumen. To evaluate the mobility of lumen-trapped  $\alpha$ TAT1-GFP, we incubated  $\alpha$ TAT1-GFP with coverslip-adhered microtubules and then washed the imaging chamber with warm buffer to remove the lattice-bound molecules, presumably leaving behind a portion of the lumen-trapped  $\alpha$ TAT1-GFP molecules. We then used fast time-lapse microscopy to collect movies of the microtubule-associated  $\alpha$ TAT1-GFP molecules that remained behind (Fig. 5B, Right). Importantly, we did not observe any fast-diffusing  $\alpha$ TAT1-GFP molecules after the washout, and, as a result, the postwashout diffusion coefficient for microtubule-associated  $\alpha$ TAT1-GFP molecules was over an order of magnitude smaller than the prewashout diffusion coefficient (Fig. 5C). This result suggests that after washout, the  $\alpha$ TAT1-GFP molecules that may have been trapped within the lumen remained behind, and that these molecules had limited

mobility, consistent with our fluorescent acetylation data and modeling work.

This result is in contrast to recent work by Szyk et al. (18), which suggested that luminal  $\alpha$ TAT1 was able to scan the length of the microtubule quickly. However, although our experimental prewashout measurements for the diffusion coefficient of  $\alpha$ TAT1 on the microtubule lattice were similar to the prewashout measurements reported by Szyk et al. (18),  $\alpha$ TAT1 has been reported to interact electrostatically with the outside of the microtubule lattice (16), and so we surmised that our prewashout diffusion coefficient largely reflected  $\alpha$ TAT1 diffusion on the outside of the microtubule. This argument is consistent with our observations of diffusing  $\alpha$ TAT1-GFP molecules “jumping” from one microtubule to another on the exterior surface of the microtubule in the prewashout movies (Fig. 5D and Movie S3).

**Acetylated Patch Length Increases with Increasing Salt Concentration.** Our results are consistent with a model in which  $\alpha$ TAT1 exhibits slow and impeded mobility inside of the microtubule lumen. This slow and impeded mobility may be due to rapid rebinding of  $\alpha$ TAT1 to densely packed acetylation sites, as well as to a slow luminal  $\alpha$ TAT1 off-rate. Therefore, we reasoned that if the  $\alpha$ TAT1 rebinding rate was suppressed and the off-rate was increased, this net decrease in affinity for the  $\alpha$ TAT1 luminal acetylation site should lead to increased  $\alpha$ TAT1 mobility within the lumen, and subsequently to longer patches of microtubule acetylation. Consistent with this hypothesis, our simulations predicted that larger mean travel distances between rebinding events  $\langle\Delta x_{lumen}\rangle$  for luminal  $\alpha$ TAT1 molecules would lead to longer simulated acetylation patch lengths (Fig. 6 A–C and SI Appendix).

To test this prediction, we noted that it has been previously demonstrated that the binding affinity of  $\alpha$ TAT1 for microtubules is suppressed at higher salt concentrations (16). Therefore, if the slow mobility of  $\alpha$ TAT1 inside of the microtubule lumen is due to rapid high-affinity binding to densely packed tubulin subunits, we predicted that by adding salt during  $\alpha$ TAT1 incubation, a net decrease in  $\alpha$ TAT1 affinity for the microtubule could lead to longer acetylation patch lengths. Thus, we performed the acetylation-TIRF experiments, but by adding different concentrations of KCl during  $\alpha$ TAT1 incubation. Strikingly, patch lengths were approximately threefold longer if the  $\alpha$ TAT1 incubation was carried out at high-salt conditions relative to our previous no-salt-added conditions (Fig. 6D and E; two-sample *t* test,  $P = 5.2 \times 10^{-12}$ ), whereas the size of  $\alpha$ TAT1 itself remained unchanged (Fig. 6E, Inset). This result supports a model in which the mobility of  $\alpha$ TAT1 within the microtubule lumen is controlled by its affinity to the densely packed acetylation sites within the lumen (Fig. 6F), and that reduced affinity in experiments with higher ionic strength allowed for increased mobility of  $\alpha$ TAT1 within the lumen.

Reduced  $\alpha$ TAT1 affinity for its acetylation binding site via increased ionic strength could explain, at least in part, the increased efficiency of  $\alpha$ TAT1 mobility in the experiments of Szyk et al. (18) compared with the data presented here. TIRF acetylation experiments in the report by Szyk et al. (18) were performed with 50 mM added KCl, which would be expected to increase acetylation patch lengths: as shown in Fig. 6E, we found that there was an approximately twofold increase in acetylation patch lengths with 50 mM added KCl compared with the “no-KCl-added” conditions in our baseline experiments.

## Discussion

On the basis of our  $\alpha$ TAT1-GFP localization data, computational simulations, biochemical experiments, and acetylation localization data, we conclude that the foremost mode of entry for  $\alpha$ TAT1 into the microtubule lumen is through the microtubule ends, or through bends and breaks in the microtubule wall. This conclusion is in contrast to the model from Shida et al. (13), which suggested that  $\alpha$ TAT1 may access the microtubule lumen through regular lattice breathing at any position along the lattice,

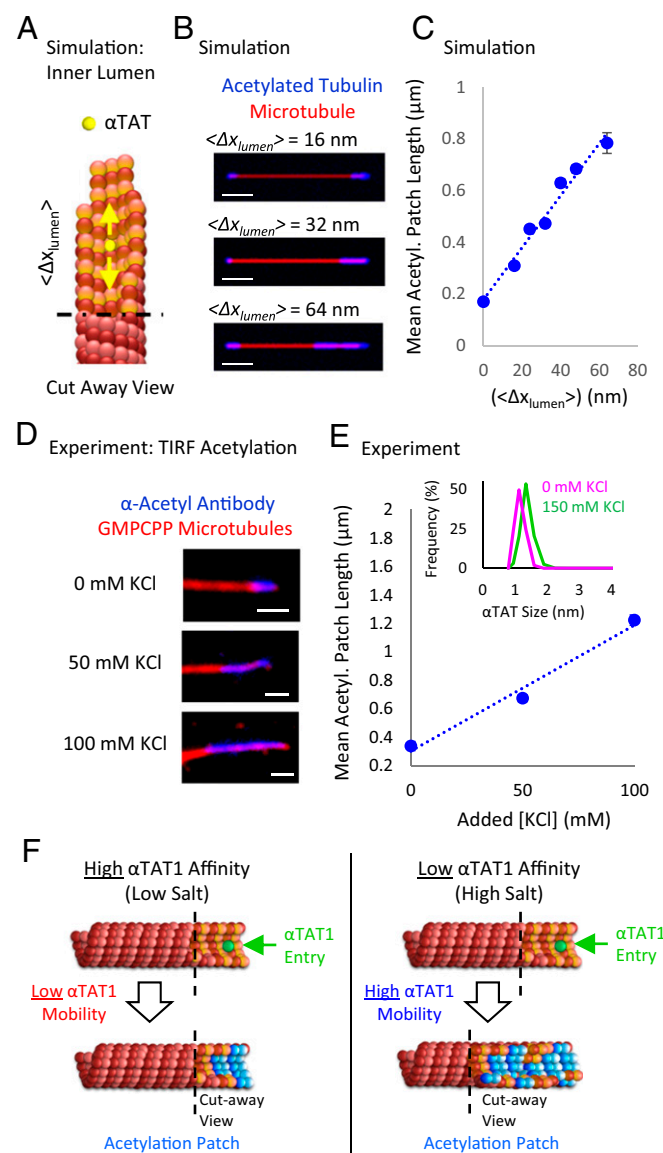


**Fig. 6.** Reduced binding affinity of  $\alpha$ TAT1 for microtubules leads to increased mobility within the lumen, and therefore increased acetylation patch lengths. (A) Schematic of  $\alpha$ TAT1 movement inside of the microtubule lumen. Yellow arrows represent the mobility of  $\alpha$ TAT1 within the lumen, which is described by the variable  $\langle\Delta x_{lumen}\rangle$ , the mean  $\alpha$ TAT1 travel distance between binding events. (B) Simulated TIRF microscopy images of acetylation patches with increasing  $\langle\Delta x_{lumen}\rangle$  for  $\alpha$ TAT1 (SI Appendix). (Scale bars: 1  $\mu$ m.) (C) Simulations predict that patch lengths will increase with increased travel distance between binding events for luminal  $\alpha$ TAT1 ( $\langle\Delta x_{lumen}\rangle$ ). (D) Example TIRF microscopy images from experiments with increasing added KCl concentration during  $\alpha$ TAT1 incubation. (Scale bars: 1  $\mu$ m.) (E) Patch lengths increase at higher KCl concentrations ( $n \geq 426$  each concentration, error bars 95% confidence intervals). (Inset)  $\alpha$ TAT1 Nanoflex size analysis (Materials and Methods), with (green line) and without (magenta line) added KCl. (F) Model for acetylation of stable microtubules in low (Left) and high (Right) salt.

but is consistent with findings from Akella et al. (12), in which the Lys40 acetylation signal formed a decreasing gradient that peaked at microtubule ends in axonemes. We also found that once  $\alpha$ TAT1 enters the microtubule lumen, it moves slowly down the lumen, and that this mobility is controlled by the affinity of  $\alpha$ TAT1 for the highly concentrated  $\alpha$ -tubulin acetylation sites within the lumen. This impeded mobility leads to concentrated patches of microtubule acetylation at the ends of stable microtubules.

Our results suggest that  $\alpha$ TAT1 enters the microtubule ends and preferentially acetylates these ends because  $\alpha$ TAT1 is not able to diffuse efficiently within the lumen. This conclusion is in contrast to recent work by Szyk et al. (18), which suggested that a high concentration of  $\alpha$ TAT1 was able to acetylate an entire microtubule almost simultaneously through longer acetylation bursts that occurred randomly along the microtubule length (18). Although one difference between our studies was in the ionic strength of the buffers, we also noted that a potentially important difference between the two studies was that we used GMPCPP-stabilized microtubules to analyze acetylation patterns on pre-formed microtubules, whereas Szyk et al. (18) used Taxol-stabilized microtubules. Both the timing and method of Taxol introduction have been shown to affect the structure of Taxol microtubules (34). Our work has demonstrated that microtubule structure, and particularly the presence of defects and openings in the microtubule lattice, would have a substantial impact on the efficiency of  $\alpha$ TAT1 in accessing and acetylating luminal acetylation sites. As shown in *SI Appendix*, Fig. S5, we found that one-step microtubule stabilization by Taxol may lead to more open, sheet-like microtubule structures, thus facilitating direct access of  $\alpha$ TAT1 to its acetylation site and potentially leading to a more disperse acetylation pattern. Therefore, differences in the microtubule stabilization technique, in addition to the experimental ionic strength, may contribute to differing acetylation patterns between this study and the study of Szyk et al. (18).

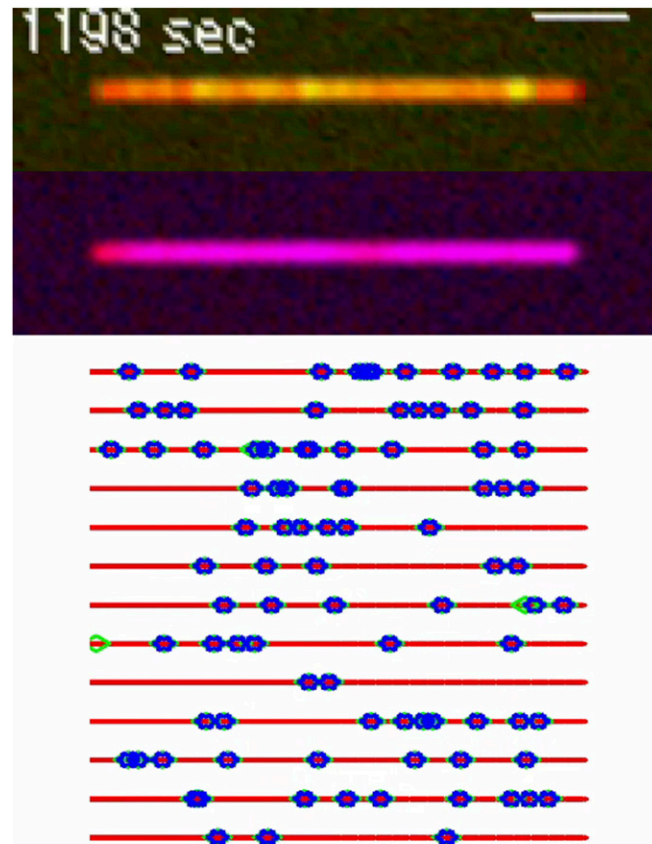
Our results are consistent with a model in which  $\alpha$ TAT1 stochastically enters microtubule ends. Thus, if  $\alpha$ TAT1 never enters a microtubule end, the microtubule could remain unacetylated, even when nearby microtubules are partially or even fully acetylated. However, in stable cellular microtubule networks, where the  $t_{1/2}$  of some microtubules is  $\sim 2.2$  h (35), such as in neurons, it is more likely that  $\alpha$ TAT1 would ultimately enter the ends of a larger fraction of the microtubules, given their long lifetimes. Then,  $\alpha$ TAT1 may be able to acetylate the stable microtubules slowly while traveling down the lumen, especially under high-salt conditions such as is present inside of cells (Fig. 6F). In addition, we demonstrated that disruption of microtubule structure leads to an increase in microtubule acetylation (Figs. 3E and 4 B–E), and that acetylation often occurs at breaks in the microtubule lattice (Fig. 4A), suggesting that microtubule bending and breaking may provide secondary  $\alpha$ TAT1 entry points to the lumen inside of cells. In cells, stable microtubule networks might naturally accumulate more lattice breaks

- Quinones GB, Danowski BA, Devaraj A, Singh V, Ligon LA (2011) The posttranslational modification of tubulin undergoes a switch from deetyrosination to acetylation as epithelial cells become polarized. *Mol Biol Cell* 22(7):1045–1057.
- Janke C, Bulinski JC (2011) Post-translational regulation of the microtubule cytoskeleton: Mechanisms and functions. *Nat Rev Mol Cell Biol* 12(12):773–786.
- Soppina V, Herbstman JF, Skiniotis G, Verhey KJ (2012) Luminal localization of  $\alpha$ -tubulin K40 acetylation by cryo-EM analysis of fab-labeled microtubules. *PLoS One* 7(10):e48204.
- Nogales E, Whittaker M, Milligan RA, Downing KH (1999) High-resolution model of the microtubule. *Cell* 96(1):79–88.
- Arce CA, Casale CH, Barra HS (2008) Submembraneous microtubule cytoskeleton: Regulation of ATPases by interaction with acetylated tubulin. *FEBS J* 275(19):4664–4674.
- Wickström SA, Masoumi KC, Khochbin S, Fässler R, Massoumi R (2010) CYLD negatively regulates cell-cycle progression by inactivating HDAC6 and increasing the levels of acetylated tubulin. *EMBO J* 29(1):131–144.
- Castro-Castro A, Janke C, Montagnac G, Paul-Gilloteaux P, Chavrier P (2012) ATAT1/MEC-17 acetyltransferase and HDAC6 deacetylase control a balance of acetylation of alpha-tubulin and cortactin and regulate MT1-MMP trafficking and breast tumor cell invasion. *Eur J Cell Biol* 91(11–12):950–960.
- Hempen B, Brion JP (1996) Reduction of acetylated alpha-tubulin immunoreactivity in neurofibrillary tangle-bearing neurons in Alzheimer's disease. *J Neuropathol Exp Neurol* 55(9):964–972.
- Outeiro TF, et al. (2007) Sirtuin 2 inhibitors rescue alpha-synuclein-mediated toxicity in models of Parkinson's disease. *Science* 317(5837):516–519.
- Godena VK, et al. (2014) Increasing microtubule acetylation rescues axonal transport and locomotor deficits caused by LRRK2 Roc-COR domain mutations. *Nat Commun* 5:5245.
- Dompierre JP, et al. (2007) Histone deacetylase 6 inhibition compensates for the transport deficit in Huntington's disease by increasing tubulin acetylation. *J Neurosci* 27(13):3571–3583.
- Akella JS, et al. (2010) MEC-17 is an alpha-tubulin acetyltransferase. *Nature* 467(7312):218–222.
- Shida T, Cuevas JG, Xu Z, Goodman MB, Nachury MV (2010) The major alpha-tubulin K40 acetyltransferase alphaTAT1 promotes rapid ciliogenesis and efficient mechanosensation. *Proc Natl Acad Sci USA* 107(50):21517–21522.
- Kalebic N, et al. (2013)  $\alpha$ TAT1 is the major  $\alpha$ -tubulin acetyltransferase in mice. *Nat Commun* 4:1962.
- Perdiz D, Mackeh R, Poüs C, Baillet A (2011) The ins and outs of tubulin acetylation: More than just a post-translational modification? *Cell Signal* 23(5):763–771.
- Howes SC, Alushin GM, Shida T, Nachury MV, Nogales E (2014) Effects of tubulin acetylation and tubulin acetyltransferase binding on microtubule structure. *Mol Biol Cell* 25(2):257–266.
- Yajima H, et al. (2012) Conformational changes in tubulin in GMPCPP and GDP-taxol microtubules observed by cryoelectron microscopy. *J Cell Biol* 198(3):315–322.
- Szyk A, et al. (2014) Molecular basis for age-dependent microtubule acetylation by tubulin acetyltransferase. *Cell* 157(6):1405–1415.
- Maruta H, Greer K, Rosenbaum JL (1986) The acetylation of alpha-tubulin and its relationship to the assembly and disassembly of microtubules. *J Cell Biol* 103(2):571–579.
- Kormendi V, Szyk A, Piszczeck G, Roll-Mecak A (2012) Crystal structures of tubulin acetyltransferase reveal a conserved catalytic core and the plasticity of the essential N terminus. *J Biol Chem* 287(50):41569–41575.
- Piperno G, LeDizet M, Chang XJ (1987) Microtubules containing acetylated alpha-tubulin in mammalian cells in culture. *J Cell Biol* 104(2):289–302.

22. Black MM, Baas PW, Humphries S (1989) Dynamics of alpha-tubulin deacetylation in intact neurons. *J Neurosci* 9(1):358–368.
23. Piperno G, Fuller MT (1985) Monoclonal antibodies specific for an acetylated form of alpha-tubulin recognize the antigen in cilia and flagella from a variety of organisms. *J Cell Biol* 101(6):2085–2094.
24. Schulze E, Asai DJ, Bulinski JC, Kirschner M (1987) Posttranslational modification and microtubule stability. *J Cell Biol* 105(5):2167–2177.
25. Webster DR, Borisy GG (1989) Microtubules are acetylated in domains that turn over slowly. *J Cell Sci* 92(Pt 1):57–65.
26. Gardner MK, et al. (2011) Rapid microtubule self-assembly kinetics. *Cell* 146(4):582–592.
27. Demchouk AO, Gardner MK, Odde DJ (2011) Microtubule tip tracking and tip structures at the nanometer scale using digital fluorescence microscopy. *Cell Mol Bioeng* 4(2):192–204.
28. Coombes CE, Yamamoto A, Kenzie MR, Odde DJ, Gardner MK (2013) Evolving tip structures can explain age-dependent microtubule catastrophe. *Curr Biol* 23(14):1342–1348.
29. Kalebic N, et al. (2013) Tubulin acetyltransferase  $\alpha$ TAT1 destabilizes microtubules independently of its acetylation activity. *Mol Cell Biol* 33(6):1114–1123.
30. Tomishige M, Vale RD (2000) Controlling kinesin by reversible disulfide cross-linking. Identifying the motility-producing conformational change. *J Cell Biol* 151(5):1081–1092.
31. Northrup SH, Erickson HP (1992) Kinetics of protein-protein association explained by Brownian dynamics computer simulation. *Proc Natl Acad Sci USA* 89(8):3338–3342.
32. Odde D (1998) Diffusion inside microtubules. *Eur Biophys J* 27(5):514–520.
33. Gupta KK, et al. (2013) Mechanism for the catastrophe-promoting activity of the microtubule destabilizer Op18/stathmin. *Proc Natl Acad Sci USA* 110(51):20449–20454.
34. Arnal I, Wade RH (1995) How does taxol stabilize microtubules? *Curr Biol* 5(8):900–908.
35. Li Y, Black MM (1996) Microtubule assembly and turnover in growing axons. *J Neurosci* 16(2):531–544.
36. Bulinski JC, Richards JE, Piperno G (1988) Posttranslational modifications of alpha tubulin: Detyrosination and acetylation differentiate populations of interphase microtubules in cultured cells. *J Cell Biol* 106(4):1213–1220.
37. Thompson WC, Asai DJ, Carney DH (1984) Heterogeneity among microtubules of the cytoplasmic microtubule complex detected by a monoclonal antibody to alpha tubulin. *J Cell Biol* 98(3):1017–1025.
38. Montagnac G, et al. (2013)  $\alpha$ TAT1 catalyses microtubule acetylation at clathrin-coated pits. *Nature* 502(7472):567–570.

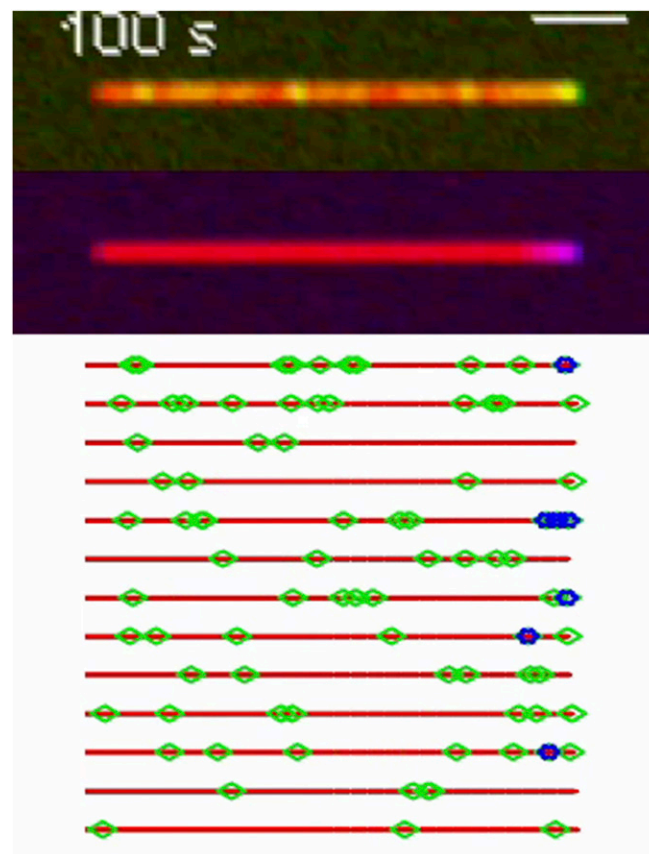
# Supporting Information

Coombes et al. 10.1073/pnas.1605397113



**Movie S1.** Simulation of real-time acetylation: lattice-entry model. This simulation demonstrates (*i*) the dynamics of simulated  $\alpha$ TAT1-GFP with a red stabilized microtubule (*Top*; microtubule, red;  $\alpha$ TAT1-GFP, green), (*ii*) the associated pattern of acetylation as viewed by a simulated antiacetylated tubulin antibody (*Middle*; microtubule, red; antiacetyl antibody, blue), and (*iii*) a schematic output of the process (*Bottom*), in which microtubule protofilaments are shown in red;  $\alpha$ TAT1 on the external surface of the microtubule is shown in green; and  $\alpha$ TAT1, which has entered into the microtubule lumen, is shown in blue. Simulation length is 20 min real time.

[Movie S1](#)



**Movie S2.** Simulation of real-time acetylation: end-entry model. This simulation demonstrates (i) the dynamics of simulated  $\alpha$ TAT1-GFP with a red stabilized microtubule (*Top*; microtubule, red;  $\alpha$ TAT1-GFP, green), (ii) the associated pattern of acetylation as viewed by a simulated antiacetylated tubulin antibody (*Middle*; microtubule, red; antiacetyl antibody, blue), and (iii) a schematic output of the process (*Bottom*), in which microtubule protofilaments are shown in red;  $\alpha$ TAT1 on the external surface of the microtubule is shown in green; and  $\alpha$ TAT1, which has entered into the microtubule lumen is shown in blue. Simulation length is 20 min real time.

[Movie S2](#)



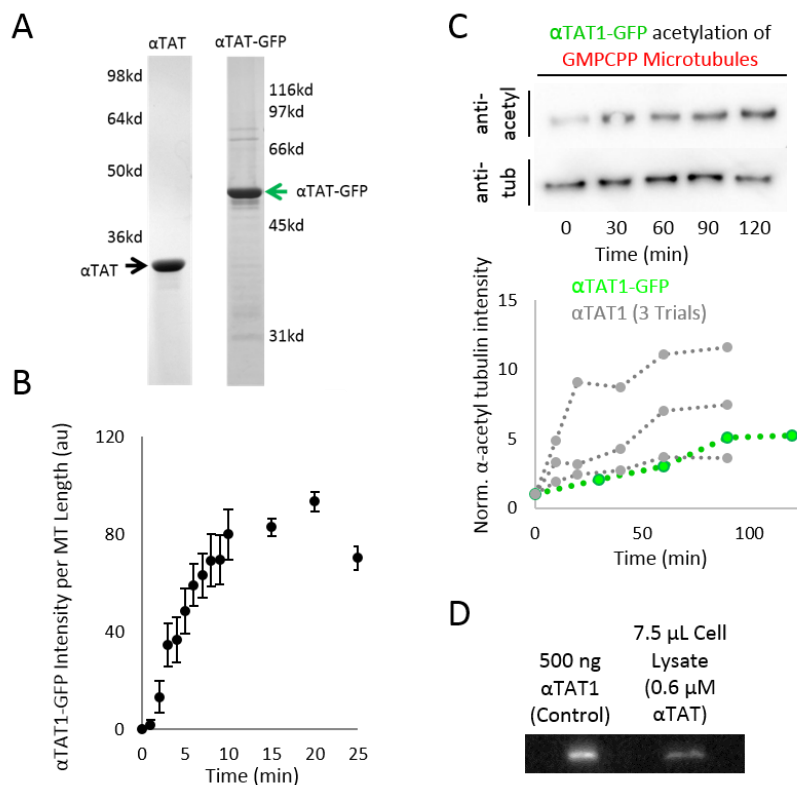
**Movie S3.** Diffusion of  $\alpha$ TAT1-GFP on GMPCPP-stabilized microtubules. The movie shows a microtubule in red, and fluorescent  $\alpha$ TAT1-GFP in green. Time-lapse images are collected every 380 ms. In this movie, motile  $\alpha$ TAT1 GFP lands on a microtubule, diffuses, and then suddenly "jumps" to a nearby microtubule, consistent with diffusion on the external surface of the microtubules.

[Movie S3](#)

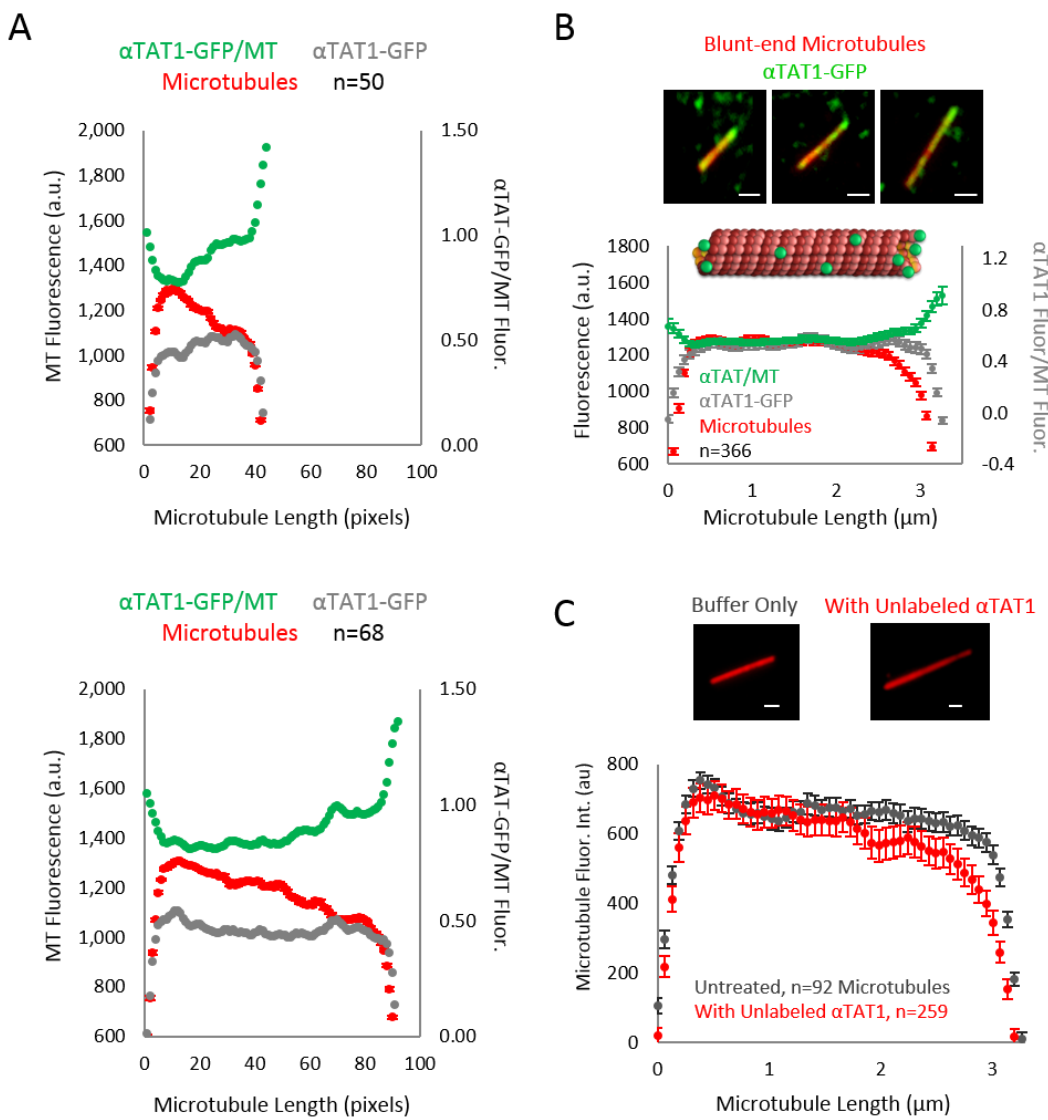
# **Mechanism of Microtubule Lumen Entry for the $\alpha$ -Tubulin Acetyltransferase Enzyme $\alpha$ TAT1**

Courtney E. Coombes, , Ami Yamamoto, Mark McClellan, Taylor A. Reid, Melissa Plooster, G.W. Gant Luxton, Joshua D. Alper, Jonathon Howard, and Melissa K. Gardner

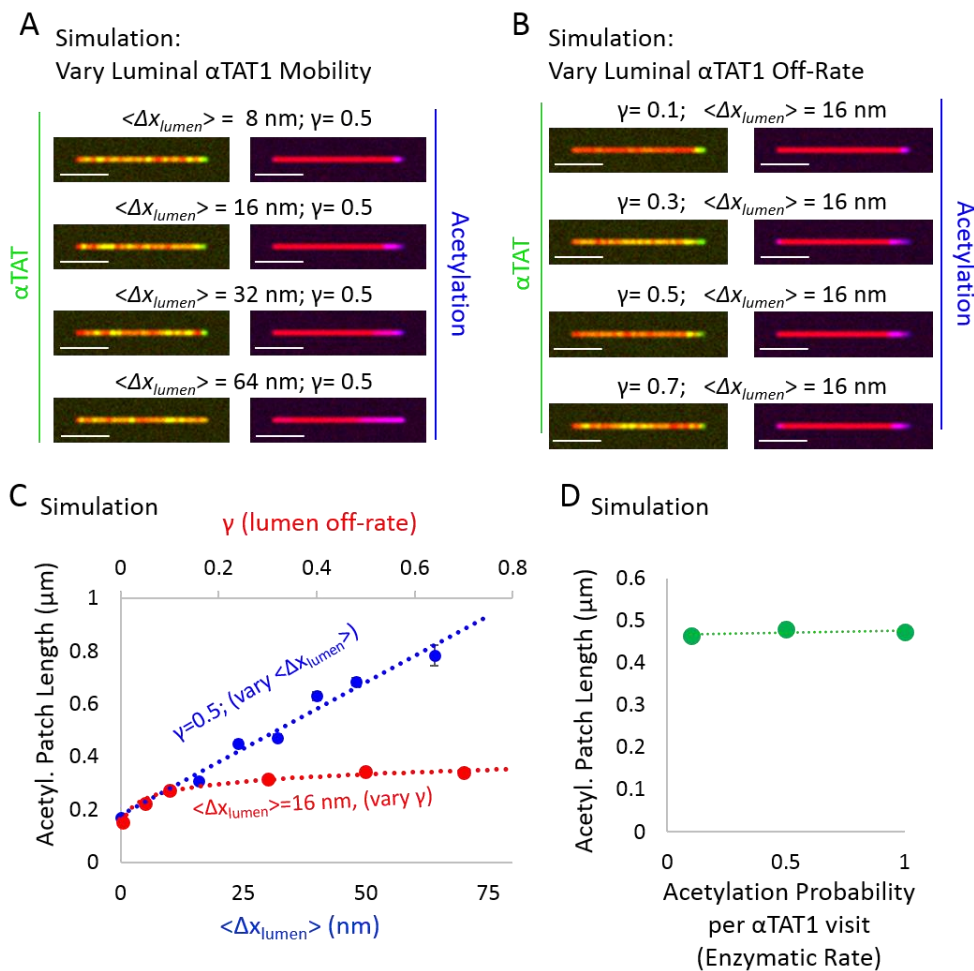
<u>Supplemental Item</u>	<u>Page No.</u>
Figure S1: Verification of unlabeled $\alpha$ TAT1 and $\alpha$ TAT1-GFP .....	2
Figure S2: $\alpha$ TAT1 Binding to Microtubules .....	3
Figure S3: Evaluation of Simulation Parameters .....	4
Figure S4: Additional Experimental Data .....	5
Figure S5: Comparison to Previous Work: .....	7
Experimental Methods.....	9
Modeling Methods.....	14
Supplemental Reference list .....	24

**Supplemental Results: Figure S1**

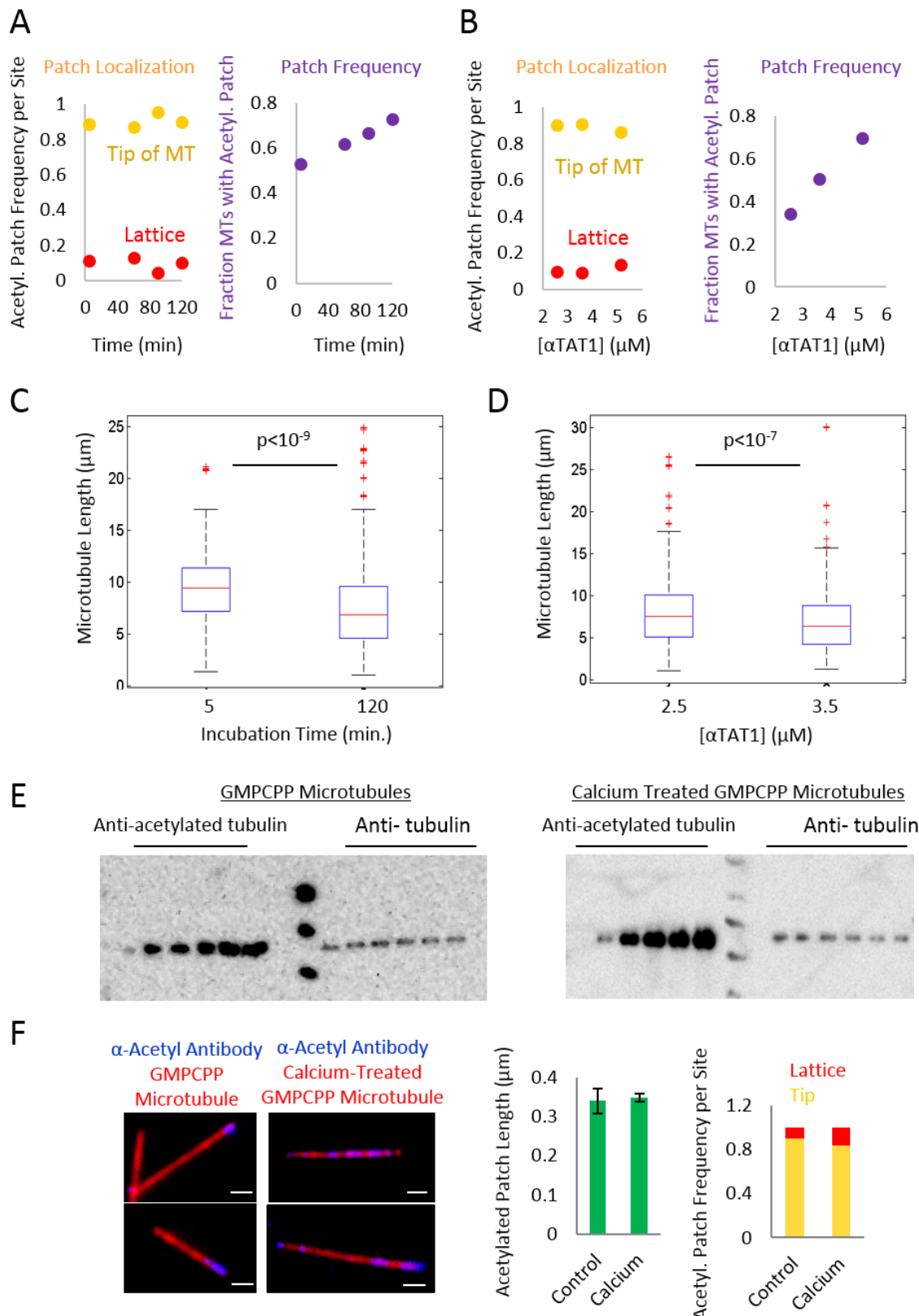
**Figure S1: Verification of unlabeled αTAT1 and αTAT1-GFP.** (A) Human αTAT1 and αTAT1-GFP protein was expressed and purified from *E. coli* cells. The two cropped Coomassie Gels demonstrate the purity of the αTAT1 and αTAT1-GFP preparations. Hydrodynamic size of proteins under experimental buffer conditions shown in Fig. 6E (inset). (B) Quantitative analysis of integrated αTAT1-GFP fluorescence intensity measured per microtubule length over increasing amounts of time after αTAT1-GFP addition to the imaging chamber ( $n > 100$  for each time point). Steady-state binding is achieved after  $\sim 15$  minutes. Kinetic analysis of this data as described in supplemental methods (below). (C) Top: GMPCPP microtubules were acetylated with αTAT1-GFP and measured from 0 to 120 minutes using western blots. Bottom: Quantitative analysis was performed by normalizing blot intensities to tubulin loading controls. αTAT1-GFP (green) and unlabeled αTAT1 (grey) acetylate GMPCPP microtubules at similar rates. (D) The concentration of αTAT1 in human RPE cells was approximated by western blot. Known concentrations of αTAT1 were blotted with an anti- αTAT1 antibody alongside cell lysate. The approximate concentration of αTAT1 in cells was  $0.6 \mu\text{M}$ , which is within the range of concentrations used in our *in vitro* experiments.

**Supplemental Results: Figure S2**

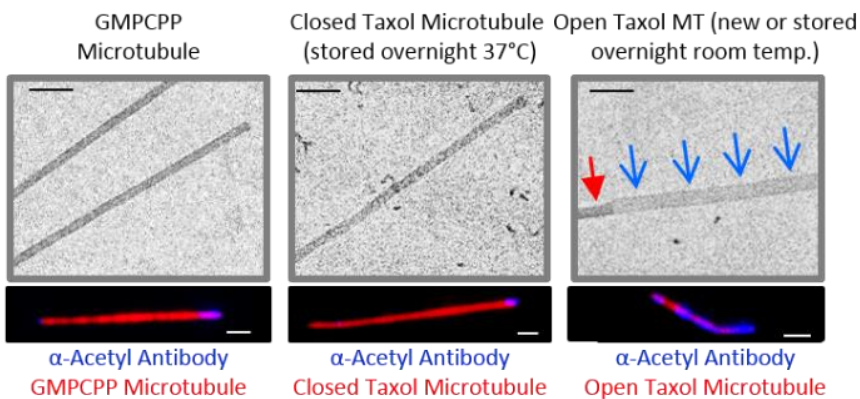
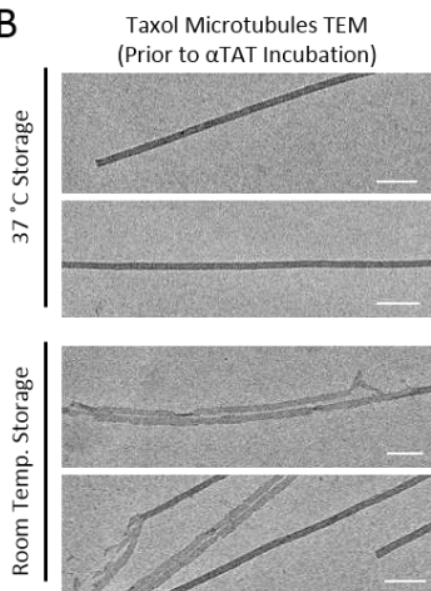
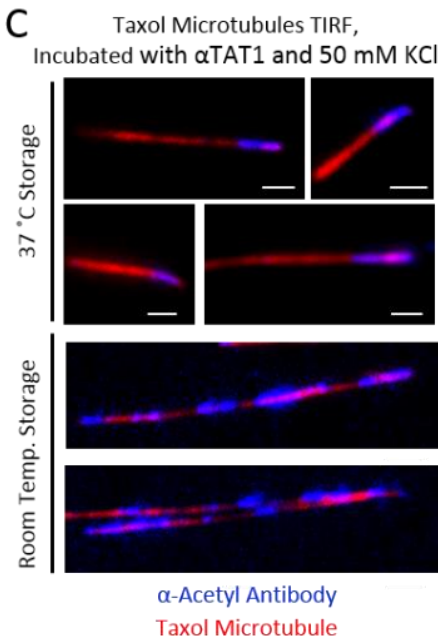
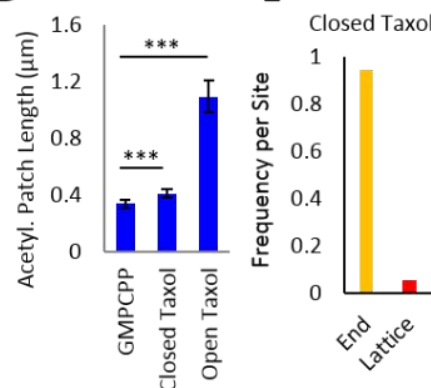
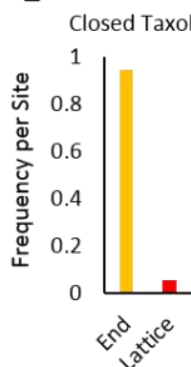
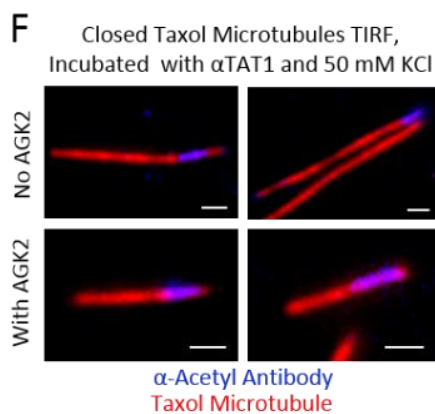
**Figure S2: αTAT1 Binding to Microtubules.** (A) αTAT1-GFP fluorescence intensity (grey), microtubule fluorescence intensity (red), and αTAT1-GFP fluorescence normalized to microtubule fluorescence (green), all as a function of position for short microtubule lengths (top), and longer microtubule lengths (bottom). (B) Top: example TIRF microscopy images of αTAT1-GFP (green) binding to blunt GMPCPP microtubules (red). Blunt microtubules were made by incubating rhodamine tubulin and GMPCPP at 37°C for 10 minutes (see methods). Bottom: αTAT1-GFP fluorescence intensity (grey), microtubule fluorescence intensity (red), and αTAT1-GFP fluorescence normalized to microtubule fluorescence (green), all as a function of position. αTAT1-GFP intensity is reduced on blunt microtubules as compared to more tapered microtubules (Fig. S2B vs Fig. 1B). (C) Top: example TIRF microscopy images of an untreated GMPCPP microtubule (left), and a microtubule treated with unlabeled αTAT1 (right) (scale bars 1 μm). Bottom: Quantitative analysis of microtubule fluorescence for untreated GMPCPP microtubules (grey), and microtubules treated with unlabeled αTAT1 (red). The plots show increased microtubule end tapering for microtubules treated with unlabeled αTAT1 (untreated: n=92, treated with unlabeled αTAT1: n=259).

**Supplemental Results: Figure S3**

**Figure S3: Evaluation of Simulation Parameters.** (A) The effect of increasing luminal  $\alpha$ TAT1 step sizes on both acetylation patch length and also  $\alpha$ TAT1-GFP localization in the simulation was qualitatively assessed. (B) Similarly, the effect of increasing the  $\alpha$ TAT luminal off-rate correction on both acetylation patch length and also  $\alpha$ TAT1-GFP localization was qualitatively assessed. (C) Quantitative analysis of patch length for simulations shown in (A) and (B): The strongest effect on patch length is the luminal  $\alpha$ TAT1 step sizes prior to rebinding ( $\langle \Delta x_{lumen} \rangle$ ) (blue line). For the luminal  $\alpha$ TAT1 off-rate, the patch lengths approach the maximal values allowed by the set value for  $\langle \Delta x_{lumen} \rangle$  when  $\gamma > 0.1$ . Therefore, low luminal off-rates can limit patch length to below the maximum value allowed by  $\langle \Delta x_{lumen} \rangle$  (red line), however, increased (long) patch lengths result from increasing step sizes prior to rebinding (e.g., by  $\langle \Delta x_{lumen} \rangle$ ), which represents travel distance prior to rebinding. (D) The rate of enzymatic activity was not directly included as a free parameter in the simulations, rather, we added a finite probability for whether the visit of an  $\alpha$ TAT1 molecule to an unacetylated tubulin dimer would result in an acetylation event. The length of the simulated acetylation patches was not sensitive to the enzymatic rate: while the patch intensity increased more slowly over time if there was a 10% probability of acetylation per visit as compared to a 100% probability, the length of the acetylation patch after a given amount of time did not depend on enzymatic rate. This is because, in the simulation, the patch length is dependent on the mobility of the enzyme to travel down the lumen, regardless of whether all visits resulted in an acetylation event.

**Supplemental Results: Figure S4**

**Figure S4: Additional Experimental Data.** (A) Acetylation patch localization and frequency as measured by TIRF microscopy on pre-formed, stabilized microtubules with increasing amounts of  $\alpha$ TAT1 incubation time (2.5  $\mu$ M  $\alpha$ TAT1), and (B) for increasing concentrations of  $\alpha$ TAT1 (30 min incubation time). Error Bars: SEM, all data points represent >400 observations in (A) and (B), and this data was used to generate the plots in Fig. 3D. (C) Microtubule lengths with increasing  $\alpha$ TAT1 incubation time (2.5  $\mu$ M  $\alpha$ TAT1) and (D) increasing  $\alpha$ TAT1 concentration (30 min. incubation). The results in Fig. 5A were normalized to microtubule length in each case to account for this effect. (E) Acetylation rates of intact GMPCPP microtubules and calcium-treated GMPCPP microtubules were compared using western blots. Western blots of acetylated microtubules and calcium treated microtubules demonstrate an increased acetylation rate on calcium treated microtubules. (F) Effect of calcium treatment on burst length and burst localization in our acetylation TIRF experiment was assessed. Only small differences were found between GMPCPP microtubules and calcium treated GMPCPP microtubules. (Control: n= 426, Calcium: n= 1307, Burst Length: Log transformed two sample t-test p=1x10<sup>-7</sup>, Burst Frequency per Site: Two sample test of proportions p=0.003)

**Supplemental Results: Figure S5****A****B****C****D****E****F**

**Figure S5: Comparison to Previous Work.** (A) Top: TEM images of GMPCPP Microtubules (left), as compared to Taxol-stabilized microtubules that were imaged after overnight storage at 37 °C (middle). Microtubule structures appear similar (scale bar 100 nm). Bottom left, center: Typical TIRF microscopy images of acetylation patches on GMPCPP microtubules as compared to Taxol microtubules with 37 °C storage (scale bar 1 μm). Top Right: TEM images of Taxol-stabilized microtubules, imaged immediately following one-step dilution into Taxol buffer. Blue arrows indicate open microtubule structure, red arrow closed microtubule structure. (scale bar 100 nm). Bottom Right: TIRF microscopy image of acetylation patch on freshly prepared Taxol microtubule (scale bar 1 μm). (B) Taxol microtubules stored at room temperature overnight had more disrupted structures than Taxol microtubules stored at 37°C. (C) This increase in disrupted microtubule structure correlated with longer and more disperse stretches of acetylation. (D) Comparative analysis of patch lengths from GMPCPP (n=426), Closed Taxol (37 °C storage) (n=249), and Open Taxol (newly prepared) microtubules (n=328). Patch lengths were substantially longer for the Open Taxol microtubules (Log transformed t test p value<1x10<sup>-6</sup>). (E) Patch localization in closed Taxol-stabilized microtubules is similar to GMPCPP microtubules. (F) We tested the effect of the SIRT2 inhibitor, AGK2, on acetylation patches using the acetylation TIRF assay. AGK2 did not substantially alter acetylation patch lengths on Taxol microtubules.

## **Experimental Methods**

### **Purification of $\alpha$ TAT1 and $\alpha$ TAT1-GFP**

A plasmid, pGEX-GST- $\alpha$ TAT1, was purchased from Addgene.org (#27101) and transformed into Rosetta high protein expression E.coli (EMD Millipore, #71397)). GFP was also ligated into this plasmid to create pGEX-GST-GFP- $\alpha$ TAT1. E. coli containing these plasmids were grown in 10ml of LB+amp+cam media at 37° overnight, subcultured 1:200 into 500ml of fresh media and grown for 3.5hr at 37° until an A600 of 0.58. IPTG was then added to 1mM final and the cultures continued growth at 18° for 16hr. Cultures were centrifuged and the cell pellets resuspended in 16ml lysis buffer (50mM Tris pH 75, 150mM NaCl, 1% triton X-100, 10% glycerol, 2mM DTT, 2mM AEBSF, 4mg/ml lysozyme and mixed at 90min at 30°. The cell suspension was then frozen drop-wise in liquid nitrogen and the frozen beads were ground multiple times in a coffee grinder. Lysate was centrifuge at 18000xg for 1hr at 4° and the supernatant was mixed with 250ul of PBS-washed glutatione-sepharose 4B beads (GE Healthcare, #17-0756-01) for 2.5hr and 4°. Beads were then washed 4x with 3ml of lysis buffer, resuspended in 1ml lysis buffer + 12ul of Prescission protease (GE Healthcare, #27-0843-01) and mixed at 4° for 20 hrs to release the  $\alpha$ TAT1 from the GST tag and beads (Fig. S1).

### **$\alpha$ TAT1 Size Analysis**

Protein size distribution was determined by measurement on a Microtrac Nanoflex particle analyzer, a device that uses dynamic light scattering of a laser in solution to determine particle size. Purified  $\alpha$ TAT1 was measured on the Nanoflex in the same buffers and concentrations that were used in the lumen diffusion analysis:  $\alpha$ TAT1 at 156 nM in Brb80 buffer + 2 mM acetyl-CoA with and without 100 mM KCl.

### ***In vitro* Microtubule- $\alpha$ TAT1-GFP Experiments, Imaging, and Analysis**

#### **GMPCPP Microtubules**

To make stabilized GMPCPP microtubules, a 45  $\mu$ L solution which consisted of 3.9  $\mu$ M tubulin (25% rhodamine-labeled, 75% unlabeled) and 1 mM GMPCPP in BRB80 was mixed and kept on ice for 5 min, then incubated at 37°C for 10 minutes to 2 hours. Following incubation, the seeds were diluted into 400  $\mu$ L warm BRB80, and 350  $\mu$ L of this dilution was spun down in an air-driven ultracentrifuge @ 20 psi for 5 min. The supernatant was discarded, and the pellet resuspended into 400  $\mu$ L warm BRB80. To further stabilize the microtubules, Taxol was added to a final concentration of 10  $\mu$ M Taxol.

#### **Construction and Preparation of Flow Chambers for Imaging**

Imaging flow chambers were constructed as in Section VII of Gell et al. 2010 (1), with the following modifications: two narrow strips of parafilm replaced double-sided scotch tape as chamber dividers: following placement of the smaller coverslip onto the parafilm strips, the chamber was heated to melt the parafilm and create a seal between the coverslips; typically only three strips of parafilm are used, resulting in two chambers per holder. Chambers were prepared with anti-rhodamine antibody followed by blocking with Pluronic F127, as described in Section VIII of Gell et al. 2010(1).

#### **$\alpha$ TAT1-GFP Binding Assay and Imaging**

A flow chamber was prepared as described above. GMPCPP microtubules were adhered to the chamber coverslip, and the chamber was flushed gently with warm BRB80. The flow chamber was heated to 28°C using an objective heater on the microtubule stage, and then 3-4 channel volumes of imaging buffer containing 110 µg/ml Glucose Oxidase, 20 µg/ml Catalase, 20 nM D-Glucose, 10 mM DTT, 0.1 mg/ml Casien, and 1% Tween-20, were flushed through the chamber. A reaction mixture containing the imaging buffer and .08 to 100 nM final concentration of  $\alpha$ TAT1-GFP (Experiments in Fig. 1 use 30 nM) was prepared, centrifuged for 5 min at 4 °C, and then the supernatant was immediately introduced into the imaging chamber, with drops left at the flow chamber ends to keep the flow chamber from drying out during imaging.

After 10 minutes,  $\alpha$ TAT1-GFP binding on GMPCPP microtubules was imaged on a Nikon TiE microscope using 488 nm and 561 nm lasers sent through a Ti-TIRF-PAU for Total Internal Reflectance Fluorescence (TIRF) illumination. An Andor iXon3 EM-CCD camera fitted with a 2.5X projection lens was used to capture images with high signal to noise and small pixel size (64 nm). Images were collected using TIRF with a Nikon CFI Apochromat 100X 1.49 NA oil objective. Images for tip structure/ $\alpha$ TAT1-GFP binding analysis were single time points only, to avoid complications from photobleaching.

#### *$\alpha$ TAT1-GFP Binding Assay Image Analysis*

The single time point images of GMPCPP microtubules with  $\alpha$ TAT1-GFP were cropped to separate each microtubule into a single image using ImageJ. Then, integrated and averaged line scans of each microtubule image were created using a MATLAB script. In each case, the microtubule was aligned with the “dim” fluorescence end on the right, and then the red and green fluorescence were plotted as a function of microtubule length from microtubule bright end to microtubule dim end. To do this, the red tubulin fluorescence was integrated along the length of each microtubule  $\pm$  256 nm above and below the microtubule centerline to account for point spread function and variability in properly finding the microtubule centerline. Then, the red fluorescence intensity was summed over the last 576 nm on both ends of the microtubule. The lower summed value was considered the “dim” microtubule end, while the higher summed value was deemed the “bright” microtubule end. Scatter plots were created by importing the integrated line scan fluorescence data into Excel.

#### *$\alpha$ TAT1-GFP Imaging to Evaluate Diffusion Coefficients*

To image diffusion of  $\alpha$ TAT1-GFP molecules, a flow chamber with stabilized GMPCPP microtubules adhered to the coverslip was prepared as described above, and a reaction mixture containing the imaging buffer and 15 nM final concentration of  $\alpha$ TAT1-GFP was then prepared and immediately introduced to the imaging chamber. Images were taken at 20 frames per second to capture diffusion of  $\alpha$ TAT1 molecules.

For wash-out experiments, the flow chamber and  $\alpha$ TAT1-GFP mixture was prepared as above, and introduced to an imaging chamber. After incubation to allow binding of  $\alpha$ TAT1-GFP to the microtubules, the imaging chamber was then flushed with imaging buffer that contained 0.1 M KCl. Then, a low salt imaging buffer (as described above) was added to the chamber. Images were taken at 20 frames per second to capture diffusion.

#### *$\alpha$ TAT1-GFP Image Analysis and Computation to Evaluate Diffusion Coefficients*

Kymographs were created from the movies using a custom MATLAB (2015a, Mathworks) script. The  $\alpha$ TAT1-GFP traces within the kymographs were analyzed for diffusion using a custom MATLAB script as follows. A region of the kymograph without GFP signal was designated as background. Next, the position of an  $\alpha$ TAT1-

GFP molecule over time was traced roughly by hand to provide a starting point for the fitting algorithm. In order to prevent nearby molecules from affecting the fitting, a width was defined outside of which all intensities are set to be equal to the median intensity of the background region defined previously. This region slides with the hand-traced center of the  $\alpha$ TAT1-GFP intensity, minimizing interfering signal while maintaining all of the signal of interest. The sub-pixel location of the  $\alpha$ TAT1-GFP was then determined through 1-dimensional Gaussian fitting of each time point of the kymograph. The diffusion coefficient was then calculated by taking the slope of the mean-squared-displacement of the position with respect to the time interval, and dividing by  $2n$ , where  $n$  is the dimensionality of the diffusion, in this case  $n$  is 1. The units were then converted from pixels and frames to  $\mu\text{m}$  and seconds, respectively, based on the known pixel size of the microscope and the frame-rate.

### ***$\alpha$ TAT1 and BSA Conjugation to Gold Beads***

$\alpha$ TAT1 and BSA were conjugated to 20nm gold beads with the Innovacoat 20nm gold particle labeling kit (Innova Biosciences, #229-0005) as per instructions, except that the  $\alpha$ TAT1 was buffer-exchanged beforehand into PBS with Microcon Ultracel YM-3 microcentrifuge filter concentrators. For labeling proteins with 1.3 nm gold particles, buffer exchanged  $\alpha$ TAT1 was reacted for 1.5 hr with mono-sulfo-NHS-nanogold 1.3 nm particle reagent as per instructions (nanoprobes #2025A) and excess particles were washed out by 2 - wash/centrifugations in Amicon Ultra 0.5ml 30k filter units, diluting with PBS.

$\alpha$ TAT1-conjugated gold beads (1.3 nm and 20 nm) were incubated with GMPCPP microtubules and Acetyl CoA (2 mM final concentration) for 20 minutes and imaged using Transmission Electron Microscopy. BSA-conjugated gold beads (1.3 nm and 20 nm) were incubated with GMPCPP microtubules and Acetyl CoA (2 mM final concentration) for 20 minutes and imaged using Transmission Electron Microscopy.

### ***Transmission Electron Microscopy***

Reaction mixtures were prepared as described for each experiment. A drop of the reaction mixture was placed on a 300-mesh carbon coated copper grid for 1 minute. At 1 minute, the grid was stained with 1% uranyl acetate for 1 minute. The stain was then wicked away with filter paper and the grid was left to dry and then stored. Specimens were observed using an FEI Technai Spirit BioTWIN transmission electron microscope. Images were recorded at 15,000X-23,000X at -3 to -5 defocus.

### ***Fluorescence Microtubule Acetylation Assay***

#### *Calcium Treated GMPCPP Microtubules*

GMPCPP Microtubules were incubated with .04 M final concentration of  $\text{CaCl}_2$  for 40 minutes at 37°C. Calcium treated GMPCPP microtubules were then adhered to an imaging flow chamber as described above. A mixture of  $\alpha$ TAT1-GFP in imaging buffer was flushed into the flow chamber and imaged as described above.

#### *Closed Taxol Microtubules*

To make Closed Taxol microtubules, a mixture composed of 33  $\mu\text{M}$  tubulin (25% rhodamine-labeled, 75% unlabeled), 1 mM GTP, 4 mM  $\text{MgCl}_2$ , and 4 % DMSO was prepared and kept on ice for 5 min, and then incubated at 37°C for 30 minutes. Following incubation, the microtubules were diluted into 990  $\mu\text{l}$  warm Taxol solution (10  $\mu\text{M}$  Taxol with Brb80) and stored overnight at 37°C. Taxol microtubules were spun down in

an air-driven ultracentrifuge @ 20 psi for 5 min and resuspended in 50  $\mu$ l warm 10  $\mu$ M Taxol Brb80 buffer before use in assays.

#### *Open Taxol Microtubules*

To make Open Taxol microtubules, a mixture composed of 33  $\mu$ M tubulin (25% rhodamine-labeled, 75% unlabeled), 1 mM GTP, 4 mM MgCl<sub>2</sub>, and 4 % DMSO was prepared and kept on ice for 5 min, and then incubated at 37°C for 30 minutes. Following incubation, the microtubules were diluted into 990  $\mu$ l warm Taxol solution (10  $\mu$ M Taxol with Brb80). To make Open Taxol microtubules, the microtubules were either used immediately, or else stored overnight at room temperature.

#### *$\alpha$ TAT1 Acetylation Assay and Imaging*

GMPCPP, Calcium Treated, Closed Taxol, or Open Taxol microtubules were adhered to flow chamber coverslips as described above. A mixture of unlabeled  $\alpha$ TAT1 (2.5-5.5  $\mu$ M, designated in text), Acetyl CoA (2 mM final concentration), KCl (0-100 mM, designated in text), and Brb80 was flown in to the chamber and incubated for 5-120 minutes (designated in text). Then, imaging buffer with CF4-88 labeled anti-acetylated tubulin (6-11B-1, Sigma Aldrich cat. #T7451-200L; 80  $\mu$ M) was flown in to the chamber as described above and imaged using TIRF microscopy as above.

#### *$\alpha$ TAT1 Acetylation of Dynamic Microtubules Assay and Imaging*

A mixture composed of 45  $\mu$ M tubulin (25% rhodamine-labeled, 75% unlabeled), 1 mM GTP, 4 mM MgCl<sub>2</sub>, 4 % DMSO, 1.8  $\mu$ M  $\alpha$ TAT1, and 2 mM Acetyl CoA was prepared and kept on ice for 5 min, and then incubated at 37°C for 30 minutes. Following incubation, the microtubules were diluted into 990  $\mu$ l warm Taxol solution (10  $\mu$ M Taxol with Brb80). The microtubules were adhered to flow chamber coverslips. Then, imaging buffer with CF4-88 labeled anti-acetylated tubulin (6-11B-1, Sigma Aldrich cat. #T7451-200L; 80  $\mu$ M) was flown in to the chamber as described above and imaged using TIRF microscopy as above.

#### *Acetylation Patch Image Analysis*

The single time point images of GMPCPP microtubules with anti-acetyl antibody were cropped to separate each microtubule into a single image using ImageJ. Then, a MATLAB script was used to measure the location and length of acetylation “patches” on the microtubules by manual clicking. In each case, the patch positions were measured relative to the bright microtubule end and the dim microtubule end, with assignment of “bright” and “dim” ends as described above. Patches that occupied the first two pixels from each microtubule end were said to occupy a “tip” site, and patches occupying any other pixels along the microtubule were labeled “lattice” sites. The patch frequencies of tip and lattice sites were calculated by normalizing the total number of patches at each site by the total available sites in each category. Patch frequency and mean number of patches per microtubules with at least one patch were calculated by manually counting patches on microtubules.

The analysis of tubulin fluorescence intensity at lattice patches was completed using a custom MATLAB script in which the average red fluorescence intensity was calculated over the entire microtubule by manual clicking at each end of the microtubule, and then the average red fluorescence intensity under a patch was calculated by manual clicking at the ends of an observed lattice patch. The ratio of red tubulin fluorescence at a lattice patch relative to the average red fluorescence along the length of the microtubule was then calculated according to:

$$\text{fluor\_ratio} = \frac{\text{patch\_flour}}{\text{MT\_flour}} \quad (1)$$

Where *patch\_flour* is the average red tubulin fluorescence intensity under an acetylation patch, and *MT\_flour* is the average red fluorescence intensity along the entire length of the microtubule. If this ratio was < 1 for a given microtubule, then the patch was classified as being in a “dim” spot on the microtubule. In contrast, if this ratio was ≥ 1, then the patch was classified as being in a “bright” spot on the microtubule.

### **Western Blot Acetylation Assay**

#### *Acetylation Reaction Mixture*

Tubulin dimers, GMPCPP microtubules, or Calcium treated GMPCPP microtubules were mixed with Acetyl CoA (2 mM final concentration), unlabeled αTAT1 (2.5 μM final concentration), and BRB80 for 90 minutes. Reactions were kept at 37 °C. Aliquots were taken from reaction mixture at 0, 10, 20, 40, 60, and 90 minutes and stored at -20°C.

#### *Shearing Acetylation Assay*

GMPCPP microtubules were mixed with Acetyl CoA (2 mM final concentration), unlabeled αTAT1 (2.5 μM final concentration), and BRB80 for 60 minutes. At 60 minutes the mixture was split into two separate mixtures. One mixture was sheared using a small diameter needle while the other mixture was not. After 120 minutes the sheared mixture was sheared a second time while the other mixture was not. Reactions were kept at 37 °C. Aliquots were taken from the unsheared mixture at 0, 60, 120, and 180 minutes and from the sheared mixture at 120 and 180 minutes and stored at -80 °C for western blotting.

#### *Cell Lysate and Known αTAT1 concentration Mixtures*

Human RPE cells were grown using standard culturing conditions (in DMEM, 10% PBS, 1% penStrep), and lysed in 5X non-reducing buffer with BME by boiling for 5 minutes. Cell lysates (1, 5, and 10μl) were loaded alongside known concentrations of purified αTAT1 (3, 37.5, and 665 ng/μl).

#### *Western Blots*

The reaction mixture aliquots were analyzed for their protein concentrations using a Nanodrop ND-1000 Spectrophotometer. Aliquots were diluted in BRB80 and PAGE buffer. The samples were resolved in 10% polyacrylamide gels and then transferred to PVDF membranes. Membranes were then blocked in 3% BSA in Tris-buffered saline with 0.15% Tween and probed with primary antibodies for anti-α-tubulin (DM1A, VWR Scientific cat.#PI62204), anti-acetylated tubulin (6-11B-1, Sigma Aldrich cat. #T7451-200L), or anti- αTAT1 (C6orf134, LifeSpan Biosciences, Inc cat. #LS-C116215). The membranes were subsequently probed with a horseradish peroxidase-linked anti-mouse secondary (Santa Cruz BioTechnology cat. #SC-2005) or anti-rabbit secondary (Santa Cruz BioTechnology cat. #SC-2004) antibody and developed using chemiluminescence.

#### *Statistical Analysis*

All reported tests were calculated in R or excel and are noted in the manuscript.

### Modeling Methods

A stochastic simulation was developed to model  $\alpha$ TAT dynamics on both the inside and the outside of the microtubule. Tables S1-S3 summarize the overall simulation behaviors and rules, including applicable variables, formulae, and parameters. Model parameters are shown in Table S4, and are based on values experimentally gathered in this study, as well as from previously published data. Simulation parameters (e.g., such as simulation duration ( $t_{\text{dur}}$  [s]), and time step size, ( $\Delta t_{\text{step}}$  [s])) are shown in Table S5. Finally, key modeling assumptions are summarized in Table S6.

Essential aspects of the stochastic model include (1) Initiation of a stable microtubule “template” at the start of each microtubule simulation; (2) calculation of on and off rates on the outside of the microtubule for each  $\alpha$ TAT1 molecule in the simulation, and then probabilistic  $\alpha$ TAT1 molecule unbinding or rebinding at random locations on the outside of the microtubule; (3) diffusion of bound  $\alpha$ TAT1 molecules which are on the outside of the lattice; (4) entry of  $\alpha$ TAT1 molecules into the microtubule lumen; (5) calculation of on and off rates on the inside of the microtubule lumen for each  $\alpha$ TAT1 molecule in the simulation, and then probabilistic  $\alpha$ TAT1 molecule unbinding or rebinding at specified locations; (6) acetylation events inside the lumen; and (7) model-convolution image generation for  $\alpha$ TAT1-GFP and acetylation antibody images. Following are details for each of these simulation activities:

#### (1) Initiation of a stable microtubule “template” at the start of each microtubule simulation

At the start of the simulation for each microtubule, a stable microtubule “template” was created, which then remained constant for the duration of each individual microtubule simulation. This was created by selecting a “tip slope” for the tip of each microtubule plus-end, according to:

$$\text{tip\_slope} = \text{abs}(\text{randn} * \text{mean\_slope}) \quad (2)$$

Where *randn* is a built-in MATLAB function which produces a Gaussian random number with mean 0 and standard deviation 1, *abs* is a built-in MATLAB function for absolute value, and *mean\_slope* is the mean taper angle at the microtubule plus end. The value for *mean\_slope* was fitted to experimental data by varying the value in simulation until the average simulated microtubule fluorescence over n=300 microtubules was similar to the experimental curve (Fig. 2A, left).

#### (2) Behaviors on the external surface of the microtubule

Simulation of  $\alpha$ TAT1 interaction with the outside of the microtubule is based on previously published data which suggests that  $\alpha$ TAT1 binds the exterior surface of microtubules, and interacts with the C-terminal tails of tubulin (2), and also on our own and previously published observations that  $\alpha$ TAT1-GFP can diffuse on the external surface of microtubules (Fig. S5 and Movie S1) (3). Thus, simulated interactions of  $\alpha$ TAT1 with the exterior of the microtubule lattice consisted of (a) binding of  $\alpha$ TAT1 on the exterior surface of the microtubule, (b) diffusion of  $\alpha$ TAT1 on the exterior surface of the microtubule, and (c) unbinding of  $\alpha$ TAT1 from the exterior surface of the microtubule. General rules for each of these activities were as follows:

- Binding of  $\alpha$ TAT1 on the exterior surface of the microtubule: The on-rate of  $\alpha$ TAT1 onto the exterior surface of the microtubule was calculated as shown in Table S1. Then, for each individual simulated  $\alpha$ TAT1 molecule, the probability of binding to the microtubule exterior was calculated from:

$$pr\_on = 1 - \exp(-k_{on,lattice}^* \Delta t_{step}) \quad (3)$$

Where  $pr\_on$  is the probability that a given  $\alpha$ TAT1 molecule would bind to a microtubule in the current time step. Thus, if a uniformly distributed random number between 0 and 1 was less than the calculated value for  $pr\_on$ , then the  $\alpha$ TAT1 molecule would attach to the microtubule. All  $\alpha$ TAT1 molecules, whether newly bound or rebinding, were attached at random locations on the microtubule, weighted by protofilament density. This is based on the assumption that there was a uniform density of  $\alpha$ TAT1 molecules around the microtubule, and that  $\alpha$ TAT1 could diffuse rapidly in solution outside of the microtubule lumen.

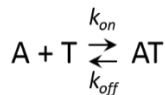
- (b) Unbinding of  $\alpha$ TAT1 from the exterior surface of the microtubule: The off-rate of  $\alpha$ TAT1 from the exterior surface of the microtubule was calculated as shown in Table S1, except in the case where an  $\alpha$ TAT1 molecule was on an exposed protofilament at the microtubule tip (defined by a position on a protofilament which is longer than the shortest protofilament in the microtubule), in which case the off-rate is calculated according to Table S3. Then, for each individual simulated  $\alpha$ TAT1 molecule, the probability of unbinding from the microtubule exterior was calculated from:

$$pr\_off = 1 - \exp(-k_{off,lattice} \Delta t_{step}) \quad (4)$$

Where  $pr\_off$  is the probability that a given  $\alpha$ TAT1 molecule would unbind from a microtubule in the current time step. Thus, if a uniformly distributed random number between 0 and 1 was less than the calculated value for  $pr\_off$ , then the  $\alpha$ TAT1 molecule would detach from the microtubule.

While a range of off-rate constants were tested to determine the impact of this value on simulation results, an order of magnitude value for the off-rate can be determined via the data in Fig. S1B, as previously described, and reproduced below (4):

For a biomolecular binding reaction of  $\alpha$ TAT1 (A) onto stabilized Tubulin polymer (T):



And at equilibrium:

$$K_{eq} = \frac{k_{on}}{k_{off}} = \frac{[AT]_{eq}}{[A]_{eq}[T]_{eq}} = \frac{1}{K_D}$$

However, for an in vitro experiment, the concentration of polymerized tubulin ([T]) remains constant, and is very small relative to the total concentration of added  $\alpha$ TAT1-GFP ( $[T] \sim 0.3$  pM (5), while free concentration of  $\alpha$ TAT1-GFP is 30 nM). Therefore, both the tubulin and the free  $\alpha$ TAT1-GFP concentrations will remain constant and equal to the equilibrium concentrations throughout the experiment, and so:

$$[A] = [A]_{eq} \text{ and } [T] = [T]_{eq}$$

Therefore, via substitution:

$$k_{on} = \frac{k_{off}[AT]_{eq}}{[A][T]}$$

Then, for the binding reaction above, the rate of formation of AT is described by:

$$\frac{d[AT]}{dt} = k_{on}[A][T] - k_{off}[AT]$$

And by substitution:

$$\frac{d[AT]}{dt} = k_{off}[AT]_{eq} - k_{off}[AT]$$

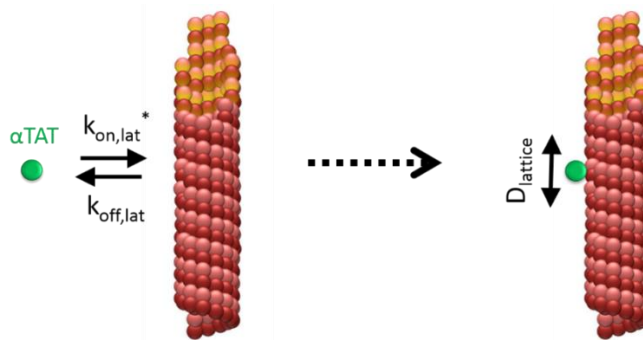
Assuming the  $[AT]=0$  at  $t=0$ , the solution to this equation is:

$$[AT]_{eq} - [AT] = e^{-k_{off}t}$$

By fitting the above equation to the data in Fig. S1B, and assuming that  $[AT]_{saturated} \sim [AT]_{eq}$ , an approximate  $k_{off,lattice}$  was estimated as  $\sim 0.2/\text{min}$ , consistent with the slow catalytic rate for  $\alpha$ TAT1 on intact microtubules (1-2/hr; (3)). However, given that previously reported  $K_D$  values for  $\alpha$ TAT1 on microtubules are suggestive of a lattice residence time of  $\sim 1$  s ( $K_D \sim 40 \mu\text{M}$  with 50 mM KCl, (3)), we tested a wide range of  $k_{off,lumen}$  values in the simulation by varying  $\gamma$ , the off-rate correction for luminal  $\alpha$ TAT1 (Fig. S5F).

- (c) Diffusion of  $\alpha$ TAT1 on the exterior surface of the microtubule. Diffusion was experimentally observed on the surface of the microtubule, with a calculated diffusion coefficient of  $0.08 \times 10^6 \text{ nm}^2/\text{s}$  (Fig. 3C and Movie S3 and (3)), consistent with previous reports of electrostatic interactions such as with the C-terminal tails of tubulin on the external surface of the microtubule (2). Thus, each bound  $\alpha$ TAT1 molecule was allowed to diffuse on the external surface of the microtubule, with step size as shown in Table S1 and constrained by the experimentally measured diffusion coefficient.  $\alpha$ TAT1 molecules which diffused to the end of a protofilament would remain at the tip of the protofilament, and did not continue to diffuse.

Table S1: Behaviors on the External Surface of the Microtubule



Behavior	Model Equation	Variables	Parameters
alphaTAT attachment to outside of microtubule lattice	$k_{on,lattice}^* = k_{on,lattice}[Tubulin]$	$k_{on,lattice}^*$ = alphaTAT on-rate for outside of microtubule lattice	$[Tubulin]$ = tubulin- polymer concentration $k_{on,lattice}$ = alphaTAT diffusion-limited bimolecular on-rate constant
alphaTAT detachment from outside of microtubule lattice	--	--	$k_{off,lattice}$ = alphaTAT off-rate from the external surface of the microtubule lattice
Diffusion of Bound alphaTAT on external surface of microtubule lattice	$(\langle \Delta x_{lattice}^2 \rangle)^{1/2} = \pm \sqrt{2D_{lattice}\Delta t_{step}}$	$\Delta x_{lattice}$ = alphaTAT diffusion step size on microtubule outside lattice	$D_{lattice}$ = alphaTAT diffusion coefficient on microtubule lattice $\Delta t_{step}$ = simulation time step size

### (3) Entry into the microtubule lumen

$\alpha$ TAT1 molecules bound to the exterior surface of a microtubule had the opportunity to enter the microtubule lumen with rules which depended on the particular lumen entry model being tested. For the end-entry model,  $\alpha$ TAT1 molecules which arrived at either end of a microtubule (as defined by arriving at a position which was past the length of the shortest protofilament), would enter the lumen with a probability as defined in Table S2. For the lattice entry model,  $\alpha$ TAT1 molecules which were bound to the lattice at any position would enter the lumen with a probability as defined in Table S2.

Table S2: Rules for Entry into the Microtubule Lumen

End Entry Model		-OR-	Lattice Entry Model
Behavior	Model Equation	Variables	Parameters
In the end-entry model, $\alpha$ TAT entry into lumen, from plus-end of microtubule	--	--	$Pr_{Enter_{plus}}$ = probability of $\alpha$ TAT which is present at microtubule plus end to enter the lumen
In the end-entry model, $\alpha$ TAT entry into lumen, from minus-end of microtubule	--	--	$Pr_{Enter_{minus}}$ = probability of $\alpha$ TAT which is present at microtubule minus end to enter the lumen
In the lattice entry model, $\alpha$ TAT entry into lumen, from a defect or other opening along the length of the lattice	--	--	$Pr_{Enter_{defect}}$ = probability of $\alpha$ TAT which is present at a position along the lattice to enter into the lumen

### (4) Behaviors on the internal surface of the microtubule lumen

Simulation of  $\alpha$ TAT1 interaction with the inside of the microtubule lumen (e.g., the  $\alpha$ -tubulin acetylation site) consisted of (a) binding of  $\alpha$ TAT1 on the interior surface of the microtubule, (b) unbinding of  $\alpha$ TAT1 from the interior surface of the microtubule, and (c) Diffusion: given that the acetylation site is on the inside of the microtubule, we assumed that  $\alpha$ TAT1 diffusion would exclusively occur in solution after unbinding, consistent with previous reports (3). General rules for each of these activities were as follows:

- a) Binding of  $\alpha$ TAT1 on the interior surface of the microtubule: The on-rate of  $\alpha$ TAT1 onto the interior surface of the microtubule was calculated as shown in Table S1. Then, for each individual simulated  $\alpha$ TAT1 molecule, the probability of binding to the microtubule exterior was calculated from:

$$pr\_on = 1 - \exp(-k_{on,lumen}^* \Delta t_{step}) \quad (5)$$

Where  $pr\_on$  is the probability that a given  $\alpha$ TAT1 molecule would bind to a microtubule in the current time step. Thus, if a uniformly distributed random number between 0 and 1 was less than the calculated value for  $pr\_on$ , then the  $\alpha$ TAT1 molecule would attach to the microtubule. We note that because the theoretical rebinding rate of  $\alpha$ TAT1 molecules is very high ( $\sim 1.7 \times 10^4 \text{ s}^{-1}$ ), the on rate of the  $\alpha$ TAT1 molecules in the simulation are limited by the time step size in the simulation, which is typically 0.01 s, to reduce computational intensity. However, a corrected free  $\alpha$ TAT1 lumen diffusion coefficient was used to compensate for the simulation time step size so that the reported travel distance between binding events for a free  $\alpha$ TAT1 molecule was correctly reflected, as described below.

In contrast to the binding events on the external surface of the microtubule,  $\alpha$ TAT1 molecules were not reattached at random locations on the inside of the microtubule, but rather were rebound very near to their previous location in the microtubule lumen. Here, given the high concentration of acetylation sites on the inside of the microtubule, we reasoned that free  $\alpha$ TAT1 diffusion in solution on the inside of the microtubule would be limited by rapid rebinding of  $\alpha$ TAT1 to nearby acetylation sites. This is due to the small volume and dense packing of tubulin subunits inside of the microtubule lumen, such that the concentration of  $\alpha$ -tubulin Lys40 acetylation site binding sites is extremely high ( $\sim 17 \times 10^3 \mu\text{M}$ ). Therefore, a typical rebinding time for a free  $\alpha$ TAT1 molecule inside the lumen with a diffusion limited biomolecular on-rate constant  $k_{on} = 1 \mu\text{M}^{-1}\text{s}^{-1}$  (6) would be  $(1/k_{on}[\text{acetylation sites}]) = 6 \times 10^{-5} \text{ sec}$ . During this time, the mean distance traveled for a free  $\alpha$ TAT molecule prior to rebinding to an acetylation site ( $\Delta x$ ) can then be calculated from:

$$(\langle \Delta x_{lumen}^2 \rangle)^{1/2} = \sqrt{2D_{solution} \Delta t_{rebind}} \quad (6)$$

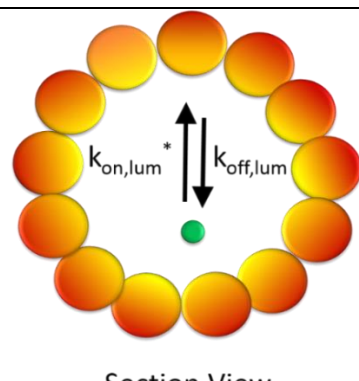
Where  $D_{solution}$  is the  $\alpha$ TAT1 diffusion coefficient in solution ( $2.6 \times 10^7 \text{ nm}^2/\text{s}$ ), and  $\Delta t_{rebind}$  is the typical rebinding time ( $\sim 10^{-5}$  sec). This leads to a predicted mean travel distance prior to  $\alpha$ TAT1 rebinding of  $\sim 50 \text{ nm}$ . For simplicity and to reduce simulation computational intensity, an adjusted diffusion coefficient,  $D_{lumen}$ , was then used to compensate for the diffusion of free  $\alpha$ TAT1 molecules within the simulation time step size,  $\Delta t_{step}$ . Thus, free  $\alpha$ TAT1 molecules in the simulation would rebinding a distance of  $\langle \Delta x_{lumen} \rangle$  away from their previously bound position inside of the lumen (Table S3). To test the sensitivity of the simulation to this parameter, the simulation predictions for a range of  $\langle \Delta x_{lumen} \rangle$  values was evaluated (Fig. 5G).

- b) Unbinding of  $\alpha$ TAT1 from the interior surface of the microtubule: The off-rate of  $\alpha$ TAT1 from the interior surface of the microtubule was calculated as shown in Table S1. Then, for each individual simulated  $\alpha$ TAT1 molecule, the probability of unbinding from the microtubule interior acetylation site was calculated from:

$$pr\_off = 1 - \exp(-k_{off,lumen} \Delta t_{step}) \quad (7)$$

Where  $pr_{off}$  is the probability that a given  $\alpha$ TAT1 molecule would unbind from an acetylation site in the current time step. Thus, if a uniformly distributed random number between 0 and 1 was less than the calculated value for  $pr_{off}$ , then the  $\alpha$ TAT1 molecule would detach from the acetylation site. To test the sensitivity of the simulation to this parameter, the simulation predictions for a range of  $k_{off,lumen}$  values was evaluated (Fig. 5G).

Table S3: Behaviors on Internal Surface-- of Microtubules



**Section View**

Behavior	Model Equation	Variables	Parameters
$\alpha$ TAT attachment to acetylation site inside the microtubule lumen; reattachment rate	$k_{on,lumen}^* = k_{on,lumen}[Ac\_sites]$	$k_{on,lumen}^*$ = $\alpha$ TAT on-rate for acetylation sites inside the microtubule lumen $k_{on,lumen}$ = diffusion limited $\alpha$ TAT bimolecular on-rate constant	$[Ac\_sites]$ = concentration of acetylation sites inside the microtubule lumen
Diffusion of Free $\alpha$ TAT inside of the microtubule lumen	$(\langle \Delta x_{lumen}^2 \rangle)^{1/2} = \pm \sqrt{2D_{lumen}\Delta t_{step}}$	$\Delta x_{lumen}$ = free $\alpha$ TAT diffusion step size inside of microtubule lumen	$D_{lumen}$ = free $\alpha$ TAT diffusion coefficient inside of microtubule lumen $\Delta t_{step}$ = simulation time step size
$\alpha$ TAT detachment from acetylation site inside the microtubule lumen	$k_{off,lumen} = \gamma(k_{off,lattice})$	$k_{off,lumen}$ = $\alpha$ TAT off-rate from inside of the microtubule lumen $\gamma$ = correction factor for off-rate of $\alpha$ TAT from exposed acetylation site relative to the external surface of microtubules	

### (5) Acetylation events for $\alpha$ TAT molecules inside the lumen

For simplicity, every acetylation site on the inside of the microtubule lumen was assumed to be non-acetylated at the start of the simulation. Then, every unacetylated site that was visited by an  $\alpha$ TAT1 molecule during the simulation was assumed to be acetylated according to the probability of acetylation ( $pr_{ac}$ ), and was flagged as such during the simulation. For all main text simulations, the probability of acetylation per visit ( $pr_{ac}$ ) was 100%, and so every visit resulted in an acetylation event. However, varying this parameter value did not change acetylation patch lengths, which primarily depended on the mobility of

$\alpha$ TAT1 within the lumen (Fig. S3D). In addition, for simplicity it was assumed that the affinity (on and off rates) of  $\alpha$ TAT1 was identical whether or not a tubulin subunit was acetylated.

#### (6) Model-convolution image creation

To visualize the localization of  $\alpha$ TAT1-GFP and, simultaneously, the fluorescent anti-acetyl antibody pattern on microtubules at the conclusion of each simulation, we performed model-convolution to generate simulated images for comparison to experiments, as previously described (7-9). Briefly, for the localization simulations, simulated images of  $\alpha$ TAT1-GFP were generated by convolving the microscope point spread function with simulated fluorescent markers at the position of each simulated  $\alpha$ TAT1-GFP molecule at the completion of a run. Here, the signal and noise were matched to experimental images, and the average fluorescence distribution curves calculated as described above.

## Model Parameters and Assumption Summary

The model parameters are summarized in Table S4, with formulae for each parameter shown in the appropriate Table S1-S3. In addition, the simulation parameters are shown in Table S5. Finally, key modeling assumptions are summarized in Table S6.

Table S4: Model Parameters

Symbol	Description	Value Range Tested	Values Used in Main Text Figures	Reference
$k_{on,lattice}^*$	$\alpha$ TAT on-rate, lattice exterior	7 s <sup>-1</sup>	7 s <sup>-1</sup>	Northrup and Erickson (1992)(6)
$k_{off,lattice}$	$\alpha$ TAT off-rate constant from exterior microtubule lattice	0.1-10 s <sup>-1</sup>	1 s <sup>-1</sup>	This study
$\langle \Delta x_{lattice} \rangle$	Bound $\alpha$ TAT diffusion step size, lattice exterior	40 nm	40 nm	Constrained by experiment (Fig. S5) and similar to Szyk et al (2014) (3)
$Pr_{enter}_{plus}$	In the end-entry model, probability of $\alpha$ TAT located at microtubule plus-end to enter the lumen	0.05	0.05	This study, fit to experimental data
$Pr_{enter}_{minus}$	In the end-entry model, probability of $\alpha$ TAT located at microtubule minus-end to enter the lumen	0.005	0.005	This study, fit to experimental data
$Pr_{enter}_{defect}$	In the lattice entry model, probability of $\alpha$ TAT located randomly along the lattice to enter the lumen	0.05	0.05	Free parameter, selected to achieve rapid steady-state
$k_{on,lumen}^*$	$\alpha$ TAT on-rate, lumen interior	10 <sup>2</sup> s <sup>-1</sup>	10 <sup>2</sup> s <sup>-1</sup>	This study, limited by simulation step size
$\gamma$	Correction to external lattice $\alpha$ TAT off-rate for lumen interior	0.1 - 1	0.3 - 1	This study, fit to experimental data
$(\langle \Delta x_{lumen} \rangle^2)^{1/2}$	Free $\alpha$ TAT diffusion step size, lumen interior	16-128 nm	16-64 nm	Range constrained by theoretical argument (Eq. 6)
$pr_{ac}$	Probability of acetylation during visit of an $\alpha$ TAT molecule to an acetylation site	0.1 – 100 %	100 %	Simulation results relatively insensitive to this parameter (Fig. S3D)

Table S5: Simulation Parameters

Symbol	Description	Values Used in Main Text Figures
$t_{dur}$	Duration of the simulation	20 min
$\Delta t_{step}$	Duration of each time step	0.01 s
$N_{\alpha TAT}$	Number of $\alpha$ TAT molecules in the simulation	100
$L_{MT}$	Microtubule Length	4864 nm

Table S6: Model Assumption Summary

Behavior	Model Assumption	Reference or Explanation
$\alpha$ TAT attachment to microtubule exterior lattice	Weighted random attachment of $\alpha$ TAT according to protofilament density	Free concentration of $\alpha$ TAT uniformly distributed in imaging chamber during <i>in vitro</i> experiments
$\alpha$ TAT behavior on the exterior microtubule lattice	$\alpha$ TAT diffuses on the external microtubule lattice	Observed experimentally and consistent with previous studies(2)
Acetylation behavior	$\alpha$ TAT enters the microtubule lattice to acetylate the $\alpha$ -tubulin dimer; arrival of $\alpha$ TAT on an interior dimer leads to acetylation	Based on previous studies(2, 3)
$\alpha$ TAT movement inside microtubule lumen	$\alpha$ TAT diffuses in solution, but rebinds quickly due to the high density of tubulin binding sites inside of the lumen	Theoretical considerations based on density of binding sites(6, 10)

**Supplemental Reference List**

1. Gell C, et al. (2010) Microtubule dynamics reconstituted in vitro and imaged by single-molecule fluorescence microscopy. *Methods Cell Biol* 95:221-245.
2. Howes SC, Alushin GM, Shida T, Nachury MV, & Nogales E (2014) Effects of tubulin acetylation and tubulin acetyltransferase binding on microtubule structure. *Molecular biology of the cell* 25(2):257-266.
3. Szyk A, et al. (2014) Molecular basis for age-dependent microtubule acetylation by tubulin acetyltransferase. *Cell* 157(6):1405-1415.
4. Bulinski JC, Odde DJ, Howell BJ, Salmon TD, & Waterman-Storer CM (2001) Rapid dynamics of the microtubule binding of ensconsin in vivo. *Journal of cell science* 114(Pt 21):3885-3897.
5. Gardner MK, Zanic M, Gell C, Bormuth V, & Howard J (2011) Depolymerizing Kinesins Kip3 and MCAK Shape Cellular Microtubule Architecture by Differential Control of Catastrophe. *Cell* 147(5):1092-1103.
6. Northrup SH & Erickson HP (1992) Kinetics of protein-protein association explained by Brownian dynamics computer simulation. *Proceedings of the National Academy of Sciences of the United States of America* 89(8):3338-3342.
7. Gardner M, Odde D, & Bloom K (2008) Kinesin-8 molecular motors: putting the brakes on chromosome oscillations. *Trends in cell biology*.
8. Gardner MK, et al. (2005) Tension-dependent Regulation of Microtubule Dynamics at Kinetochores Can Explain Metaphase Congregation in Yeast. *Molecular biology of the cell* 16(8):3764-3775.
9. Sprague BL, et al. (2003) Mechanisms of Microtubule-Based Kinetochore Positioning in the Yeast Metaphase Spindle. *Biophysical journal* 84(6):1-18.
10. Odde D (1998) Diffusion inside microtubules. *Eur Biophys J* 27(5):514-520.